Semiconductor Science and Technology

TOPICAL REVIEW • OPEN ACCESS

Strain and stress effects on single crystal-supported titania and related nanostructures

To cite this article: Chi Lun Pang 2020 *Semicond. Sci. Technol.* **35** 113001

OPEN ACCESS
IOP Publishing
Semiconductor Science and Technology
Semicond. Sci. Technol. **35** (2020) 113001 (29pp)
https://doi.org/10.1088/1361-6641/ab9faa

Topical Review

Strain and stress effects on single crystal-supported titania and related nanostructures

Chi Lun Pang

Surface Science Research Centre and Department of Chemistry, University of Liverpool, Liverpool L69 3BX, United Kingdom

Diamond Light Source, Harwell Science and Innovation Campus, Oxfordshire OX11 0DE, United Kingdom

E-mail: chi.pang@liverpool.ac.uk

Received 30 March 2020, revised 25 May 2020
Accepted for publication 24 June 2020
Published 22 September 2020

Abstract

The properties of materials can be altered by introducing strain. For instance, the critical temperature of superconductors has been raised as has the Curie temperature of ferroelectric materials. As TiO_2 is the most studied single crystal metal oxide, it is highly desirable to understand how strain might be used to tune its properties. Theoretical calculations indicate that the band gap of anatase TiO_2 may be lowered, which would remove one of the roadblocks to its wider use as a photocatalyst. Surface defects on rutile TiO_2 are responsible for a large part of its reactivity and the nature of these may also be affected by strain according to calculations. In this review, the introduction of strain and its effect on reactivity will be examined. The strain in the most part arises from lattice mismatch in the growth of TiO_x films on various substrates although cases where TiO_2 is the substrate are also included as is the implantation of Ar clusters in the subsurface of TiO_2.

Keywords: strain, stress, TiO_2, oxides, ultra-thin films

(Some figures may appear in colour only in the online journal)

1. Introduction

It has long been known that strained materials can change their properties, such as their (super) conductivity [1–3] reactivity [4, 5], electronic structure [6], magnetic [7], and ferroelectric behaviour [7, 8].

While materials can be strained by applying direct external stress [9–11], by far the most common way that strain is imparted is by growing a thin film on some other substrate. It should be noted that the term thin film does not imply a continuous layer and in many cases, it is flat-topped nanoparticles that develop.

The lattice mismatch between the thin film and the substrate often forces the film to grow with a compressed or expanded lattice. This type of lattice strain engineering has been a particularly important topic of study for the perovskite oxides which are composed of two different cations, A and B, with stoichiometry ABO_3, and the related Ruddlesden–Popper oxides ($A_{n+1}B_nO_{3n+1}$). What makes the perovskites such a rich class of materials for such study is the large range of cations that can be fit into the stucture so that films of one

perovskite can be grown on top of an enormous range of other perovskites [12].

Thin films of TiO_2 have also been extremely well studied lately. Unlike on the perovskites, the TiO_2 films are not isostructural with their substrates except in a small minority of special cases. Instead, substrates are often chosen so as to match their unit cells closely to known native TiO_2 phases in order to grow thin film mimics. In this way, Mo(110) [13], Ag(100) [14], and W(100) [15–19] were selected for the growth of rutile TiO_2(110) and $SrTiO_3$(001) and $LaAlO_3$(001) were selected for the growth of anatase TiO_2(001) [20–29]. Despite these films being grown ostensibly to act as mimics of the native phases, the imperfect matching of these substrates inevitably leads to strained films and this forms the topic of section 2.1.

Other substrates chosen for the growth of TiO_2 or TiO_x films (where $1 < x \leqslant 2$) are not closely lattice-matched to any native phases of TiO_2. While some native phases seem to grow anyway [30–32], more common is the growth of novel structures, the subject of section 2.2. Due to the range of lattice mismatches possible depending on the chosen substrate, the strain on these novel structures can also be tuned and in some cases, these novel structures have periodic strain structures that have been exploited to template the growth of metal nanoparticles and organic molecules [33–35]. The reactivity and templating effects of these thin films will be reviewed in section 2.3.

Sections 3 and 4 will be devoted to the role of strain in supported nanoparticles and embedded nanoparticles. While supported TiO_2 films can be strained due to the presence of the support, the reverse is also true when TiO_2 acts as the support. The study of metals supported on oxides such as TiO_2 have been extensively studied due the importance of such systems in catalysis [36, 37]. Recent studies show that the TiO_2 substrate can impart strain onto the supported nanoparticles, changing their reactivity to CO molecules [38, 39]. Strain can also be introduced into a material by implanting objects beneath the surface. When Ar was embedded into rutile TiO_2(110), this led to strained bumps at the surface. Due to the strain, these bumps have a different reactivity being devoid of surface oxygen vacancies and being unfavourable sites for hydroxyls [40–42].

In section 5, stress- and strain-induced changes in physical and chemical properties will be reviewed. On rutile TiO_2(110), DFT calaculations show that introducing strain in rutile can change the type of oxygen vacancies (O-vacs) at or near the surface [43–45] as well as their transport properties [45]. As oxygen vacancies play a key role in many surface reactions [46–48] the ability to tune them provides a route to control the surface reactivity. Interestingly, the levels of strain used in these calculations was reached in some of the experimental studies described in section 2.1.1. These calculations may also explain the absence of surface oxygen vacancies in the bumps disussed in section 4.

DFT calculations indicate that the band gap of anatase can be substantially reduced by introducing strain [49–51]. This provides a significant motivation to study such strained films given the relatively large band gap of TiO_2 is one of the roadblocks to its wider use as a photoctalayst [52–54]. Experiments seem to corroborate these calculations, with a strained anatase film grown on $SrLaGaO_4$(001) displaying a reduced band gap compared with a virtually unstrained film grown on $LaAlO_3$(001) [55]. Likewise, strained free-standing anatase-like nanoparticles had reduced band gaps compared with their unstrained counterparts [56]

Strain effects have been reported in a variety of titania nanostructures including supported nanoparticles, thin films, free-standing nanoparticles/powders [56, 57], as well as nanowires, rods, and belts [58–61]. In this review the main focus will be on single crystal-supported nanostructures, although some related structures are also discussed when particularly relevant [56]. In all reported studies, sample preparation and analysis have been performed in ultrahigh vacuum unless otherwise noted.

2. Thin oxide films

2.1. Films as mimics of native phases

Thin metal oxide films supported on metal substrates are an important class of materials that have received a great deal of attention for a variety of reasons [62–64]. For example, by using such films as mimics of their insulating counterparts, some of the experimental difficulties that arise from studying insulators can be circumvented. In this way, measurements such as scanning tunnelling microscopy (STM) and x-ray photoemission electron microscopy (XPEEM) that depend on conductive samples become possible [65–67]

2.1.1. Rutile. TiO_2 is extensively studied on account of its technological importance in applications such as solar cells and self-cleaning materials [68–70]. As the most stable rutile termination, most attention has been focused on the (110) surface [46–48] which is depicted in figure 1. The surface is characterised by rows of 5-fold coordinated Ti (Ti_5) which alternate with rows of bridging O (O_b).

Despite this vast body of work on rutile TiO_2(110), there are only a few studies of thin TiO_2(110) films. This is largely because the native rutile crystal can be made semiconducting by reduction so that charged-particle techniques including STM and XPEEM can already be used. Nevertheless, there are some cases where a thin film is highly desirable. For instance, limiting the thickness of the rutile film to a few layers allows bulk techniques such as electron paramagnetic resonance [71] and resonant inelastic x-ray scattering to be applied in a surface-sensitive manner [72].

Following the early work of Atrei *et al* [73] where rutile TiO_2(110) films were shown to grow on a $Ni_{94}TiO_6$(110) alloy, several groups have reported the formation of rutile TiO_2(110) on other metal substrates including pure Ni(110) [74–77], Mo(110) [13], Ag(100) [14], and W(100) [15–19]. In some work, the W(100)-O(2×1) reconstruction is employed because it can be prepared at much lower temperatures and leads to the same TiO_2(110) films.

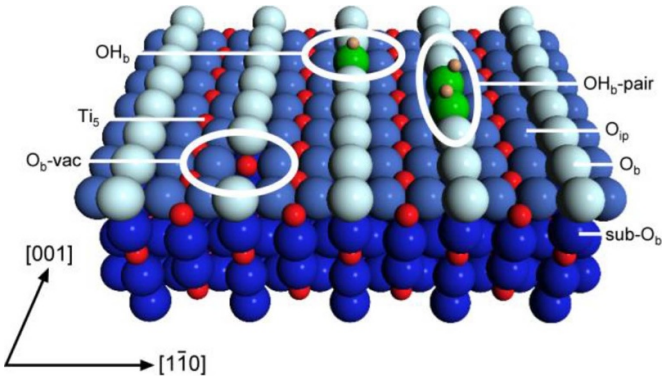

Figure 1. Ball model of the rutile TiO_2(110) surface. Blue and red spheres denote lattice O and Ti, respectively. The light blue spheres are O_b atoms, which lie in the [001] azimuth of the substrate. Parallel Ti rows that lie between the O_b rows are Ti_5 atoms. Bridging oxygen vacs (O_b-vacs) and bridging hydroxyl (OH_b) species are circled as are bridging O species (O_b), sub-bridging O (sub-O_b), and in-plane O (O_{ip}).

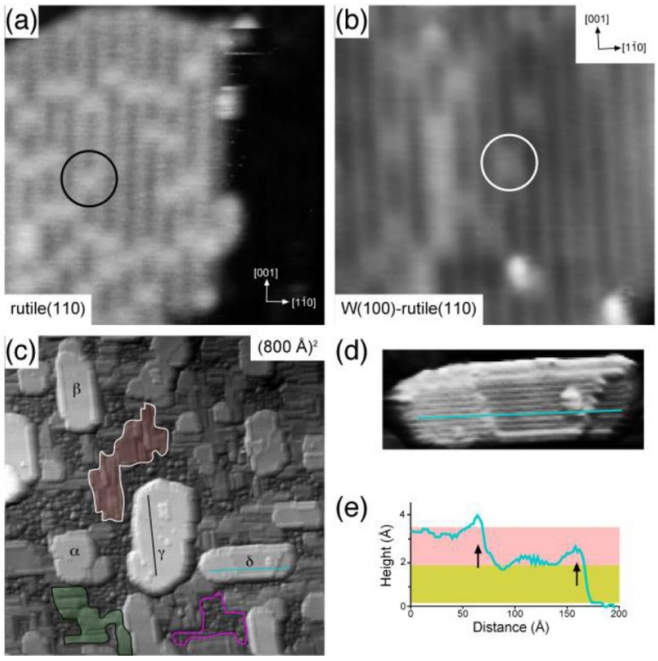

Figure 2. (100 Å)^2 STM images taken from (a) the native rutile TiO_2(110) surface and (b) the rutile TiO_2(110) film grown on W(100)-O(2 × 1). (c) (800 Å)^2 STM image of the rutile film grown on W(100)-O(2 × 1). (d) Magnified view of island δ. (e) Line profiles taken along the blue line shown in (d). The yellow and pink shading indicate heights of 1.6 Å and the arrows show the position of steps. Reprinted with permission from [19]. Copyright (2013) American Chemical Society.

Evidence for this termination of rutile TiO_2(110) comes from photoelectron diffraction (PhD), low energy electron diffraction (LEED), and vibrational spectroscopy, as well as high resolution STM. Figure 2(a) shows such an example of a high resolution STM image taken from the native rutile TiO_2(110) surface alongside that from a W(100)-O(2 × 1)-supported island in figure 2(b) [19]. Both images are characterized by bright rows which arise from Ti_5 ions and dark rows which arise from O_b. Point defects which may be bridging O vacs (O_b-vac) or bridging hydroxyls (OH_b) appear between the bright rows. In larger scale STM images, it can be seen that rather than growing as a continuous film, TiO_2(110) islands grow as discrete islands (on those substrates tested so far) as shown for TiO_2(110) on W(100)-O(2 × 1) in figure 2(c).

As similar TiO_2(110) films have been grown on a number of substrates, there is an opportunity to examine the effect of the lattice misfit (see table 1) between the substrate and the film. The W(100)-O(2 × 1) substrate was chosen specifically to minimize the lattice misfit in an attempt to grow a TiO_2(110) mimic [15–19]. W(100) has a square lattice with lattice parameter of a_W = 3.16 Å. TiO_2(110) has lattice constants of a_{TiO_2} = 6.49 Å and b_{TiO_2} = 2.96 Å, so in a simple (2 × 1) coincidence cell, a_{TiO_2} would compress by 2.6% to be equal to 2 × 3.16 Å (i.e. 6.32 Å) and b_{TiO_2} would expand by 6.3% to be equal to 3.16 Å. Analysis of the LEED pattern of TiO_2(110) on W(100) shows that a_{TiO_2} and b_{TiO_2} are instead both incommensurate, retaining the periodicity of the native rutile surface.

The situation is different on Ag(100) where b_{TiO_2} of the rutile film is commensurate. With a_{Ag} being 2.89 Å, this only requires a compression of 2.4%, whereas a_{TiO_2} would require a compression of 10.9% to match so that a_{TiO_2} was found to be incommensurate [14].

Atrei *et al* [14] rationalized their observation on Ag(100) by employing calculations using density functional theory (DFT). In these calculations, rather than compressing a_{TiO_2} to be coincident with $2a_{Ag}$, they formed coincident lattices where $5a_{Ag}$ and $7a_{Ag}$ were coincident with $2a_{TiO_2}$ and $3a_{TiO_2}$, respectively.

Table 1. Lattice constants, a and b, of rutile and the various substrates. 2 a is also listed for the substrates as this is the closer match with b_{TiO_2}.

	a (Å)	2a (Å)	b (Å)
Rutile (110)	6.49		2.96 [15]
Ag(100)	2.89	5.78	2.89 [14]
Mo(110)	3.14	6.28	2.72 [78]
W(100)	3.16	6.32	3.16 [15]
Ni(110)	3.52	7.04	2.49 [74]

This reduces the strain considerably. Nevertheless, the strain remained high: +9.8% for $a_{TiO_2}$and −1.7% for b_{TiO_2} in the (5 × 1) coincidence cell and +2.5% for a_{TiO_2} and −1.7% for b_{TiO_2}in the (7 × 1) coincidence cell. (Notice that these percentages differ slightly from experimentally-derived values due to the small differences in the calculated lattice constants). The strain energy, ΔE_S was calculated at 0.09 and 0.03 eV per TiO_2 unit for the (5 × 1) and (7 × 1) models, respectively. Even for the (7 × 1) model, which has a considerably lower strain, this is about a third of the adhesion energy of the TiO_2 layer which was −0.10–0.12 eV per TiO_2 unit. It is this energy penalty which prevents the film from being commensurate in the a_{TiO_2} direction. When the strain is removed from a_{TiO_2}, ΔE_S becomes virtually negligible.

The lattice parameters for Ni(110) are quite far from rutile TiO_2(110) in both directions so as one would expect, the film is not commensurate in either direction [73–77]. For Mo(110),

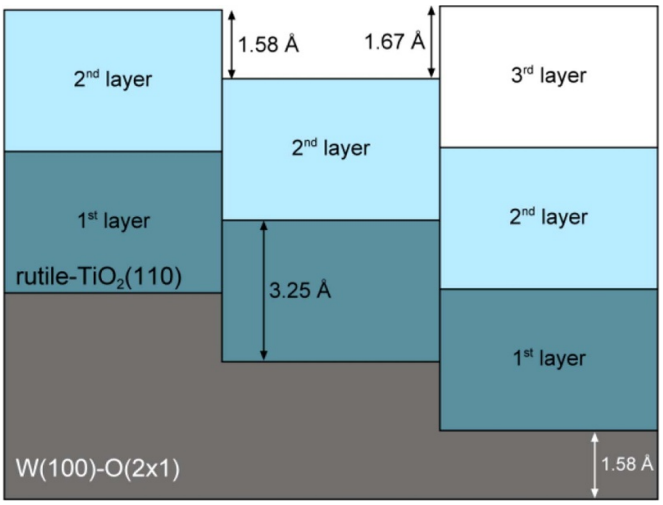

Figure 3. Schematic model showing two of the steps closest to 1.6 Å in height that can arise on the rutile TiO_2(110) island by stacking TiO_2 units onto a W(100)-O(2×1) substrate. Units of TiO_2(110) are 3.25 Å in height, and steps on the W(100)-O(2×1) substrate are 1.58 Å high. Reprinted with permission from [19]. Copyright (2013) American Chemical Society.

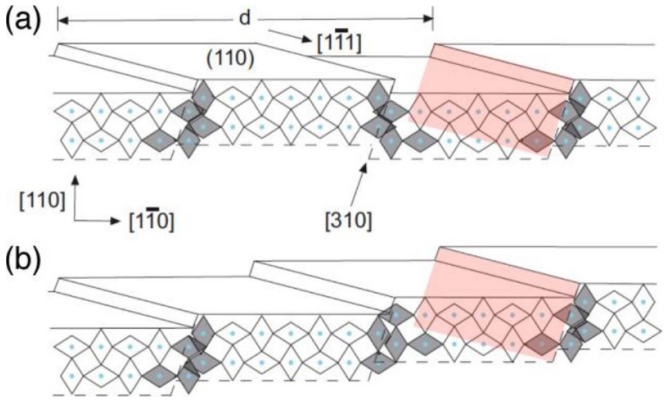

Figure 4. Schematic representation of CSPs intersecting the rutile TiO_2(110) surface. Blue circles represent Ti atoms, and rhombi indicate their pseudo-octahedral co-ordination with oxygen. Examples of CSPs with (132) orientation are indicated by pink shading. These planes intersect the surface (110) along the [1$\bar{1}$1] direction. The rhombi which form the CSPs are shaded grey. The CSPs induce half-height steps at the TiO_2(110) surface resulting in (a) an 'up-down' half-height step arrangement and (b) a 'staircase' half-height step arrangement. The periodicity between the up-down pairs, *d*, is indicated. Reprinted with permission from [77]. Copyright (2007) American Chemical Society.

three rotation domains of TiO_2(110) were observed separated successively by 120°. Although a_{TiO_2} was measured to be 6.5 Å in STM, details of the orientation of the film with respect to the substrate were not reported [13].

While we have discussed strain and misfit in the lateral direction, for W(100)-supported TiO_2(110), there is a particular consequence of the vertical misfit [19]. Figure 2(d) shows a magnified view of island δ taken from the image in figure 2(c). The line profile in figure 2(e) shows two steps (indicated with arrows in the figure), both of which have heights of about ~1.6 Å. This is significantly lower than the ~3.25 Å step height of a perfect bulk-truncated surface. A step height of ~1.6 Å can be obtained by considering a rutile TiO_2(110) island originating from different W(100) terraces as shown in figure 3. Such an island could have a range of step heights that take into account the W(100) step of 1.58 Å [79]. Two of these heights are very close to the ~1.6 Å measured: (i) a step edge that directly reflects the substrate step height (1.58 Å) and (ii) a step edge that is equivalent to one step of W(100)-O(2×1) subtracted from one step of TiO_2(110), giving a step height of 1.67 Å.

The heights of these steps are about half that of a normal TiO_2(110) step, and such half-height steps are characteristic of step edges in the presence of crystallographic shear planes (CSP). Such CSPs have been observed previously on both native rutile TiO_2(110) surfaces [80–83] and a rutile TiO_2(110) film grown on Ni(110) [77]. Normally, CSP formation is caused by reduction of the crystal. As the concentration of O-vacs increases, they order into specific planes that result in the crystal collapsing by slipping half a unit cell along the CSP, as shown in figure 4. Both step edges on island δ run in the <111> directions and CSP intersections with (110) have been found along these <111> directions [77, 80–83].

Usually when the density of CSPs is high, arrays of CSP steps form at the surface leading to an 'up-down' or 'staircase' arrangement as shown in figure 4 [77, 80, 83]. In the film of figure 2, the CSPs are far less dense with islands only containing one or two of them. As such, it was suggested that rather than being formed by reduction of the crystal, the CSPs arise as a way of accommodating the lattice strain introduced by the W(100) substrate.

The growth of rutile TiO_2(100) has been reported on several substrates. A very clear-cut example is the film supported on Au(100) [84]. The LEED showed that the short side of the TiO_2 lattice is commensurate with the Au(100) surface from which the lattice parameters were derived as $a = 4.6$ Å and $b = 2.9$ Å. This compares very well with the dimensions of the rutile TiO_2(100)-(1×1) lattice with $a = 4.59$ Å and $b = 2.96$ Å. This corresponds to just a 0.2% expansion in *a* and a 2.1% compression in *b*. Even though this rutile TiO_2(100) film is a native-like phase, on single crystals, the (1×1) phase has only been unambiguously observed co-existing with metastable (1×3) phases [85] because the tendency is to reconstruct to (1×3) or higher ($1 \times 2n + 1$) phases [48, 86–88]. The ability to grow such a (1×1) film here therefore allows a rare opportunity to assess the reactivity of this unreconstructed face.

There is also evidence for the growth of rutile TiO_2(100) on a number of hexagonal lattices, namely a thin film of Al(111) [89], α-Al_2O_3(0001) [89–91], Pt(111) [32, 92], and Au(111) [31, 93]. On Al(111), itself supported on Si(111), x-ray diffraction (XRD) showed that rutile TiO_2(100) grows with *a* parallel to Al[$\bar{2}$11] and *b* parallel to Al[0$\bar{1}$0] with three equivalent rotation domains. To form a coincident lattice, this requires an expansion of 7.5% in *a* and a compression in *b* of 3.1%. Rutile TiO_2(100) also grows on α-Al_2O_3(0001) with three rotation domains, *a* being parallel to α-Al_2O_3[$\bar{2}$110] and *b* parallel to α-Al_2O_3 [01$\bar{1}$0]. In this case for a coincident lattice,

an expansion in a of 3.6% and a compression of 7.7% in b is required.

On Pt(111) evidence for the growth of the rutile TiO_2(100) phase comes from PhD, LEED, and STM [32, 92]. A local (1 × 2) motif can be seen in STM images which also matches rather diffuse LEED spots. This unit cell has dimensions of 4.9 Å × 3.15 Å which is a reasonably close match to the rutile TiO_2(100) unit cell size requiring an expansion in a and b of 6.3 and 6.0%, respectively. A larger superlattice with (7 × 1) symmetry can also be observed in STM. Simulations of the (7 × 1) LEED pattern produced a star-like appearance due again to the presence of three rotation domains. Although this pattern was not observed in the experimental LEED, a fast fourier transform (FFT) of a high resolution STM image reproduced the star-like appearance.

On Au(111), hexagonal (or pseudohexagonal) islands were observed that were assigned to rutile TiO_2(100) [93]. The evidence comes from two geometrical measurements in STM. The step height within an island was 2.3 Å, almost identical to that expected between (100) planes and a row structure could be observed with a periodicity of 9.0–9.5 Å, consistent with a rutile TiO_2(100) (1 × 2) reconstruction. On rutile single crystals, reconstructions have been observed but only for (1 × 3) or higher (1 × 2 n + 1) phases in UHV [46, 86–88]. The different behaviour might arise from different energetics related to the thinness of the film or some interaction with the substrate.

This assignment to TiO_2(100) was supported by Ragazzon *et al* [31], although the (1 × 2) reconstruction was not observed, perhaps due to a different film preparation method. They too measured step heights consistent with rutile TiO_2(100). In addition, LEED patterns were observed which were basically identical with those generated by the LEED simulations and FFT images of Cavaliere *et al* for the Pt(111)-supported film [32], the only difference being that in the case of Au(111) an (8 × 1) unit cell is found. The rectangular unit cell measured in LEED is 23.8 Å × 5.0 Å, which corresponds to a TiO_2(100) unit cell with a expanded by 8.2% to 5.0 Å and b expanded by just 0.5% to 2.98 Å (unstrained within the reported error). These rutile phases on Au(111) and Pt(111) will be referred to as the star phases hereafter and their reactivity towards water will be shown in section 2.3 to be similar to rutile TiO_2(100) in line with the assignment of the star phase [94, 95].

2.1.2. Anatase. While there has been extensive study of rutile TiO_2, particularly the most stable (110) face, in many (but not all) applications, anatase is the more active polymorph [96, 97]. Until recently, good quality single crystal anatase samples were not readily available and this has limited such studies in the past [98]. As such, there has been a significant demand for thin film mimics. Despite being the most stable face of anatase, there are very few studies of thin (101) films [20] due to the difficulty of finding suitable substrates with near lattice matches. Instead, nearly all thin films for anatase have focused on the (001) face where there is a near lattice match with $SrTiO_3$(001) and $LaAlO_3$(001), which have a perovskite and strained perovskite structure, respectively [20–29]. These perovskite (-like) substrates have square (or pseudo-square) in-plane lattices as does the anatase (100) surface and the lattice parameters are shown in table 2.

Table 2. Lattice constants of anatase and the Ruddlesden–Popper/Perovskite oxide substrates.

Substrate	a (Å)	c (Å)
Anatase	3.785 [99]	9.51
$YAlO_3$	3.71 [100]	
$LaAlO_3$	3.78 [22]	
$SrLaGaO_4$	3.84 [55]	
$NdGaO_3$	3.86 [100]	
$(LaAlO_3)_{0.3}$-$(Sr_2AlTaO_6)_{0.7}$	3.87 [100]	
$SrTiO_3$	3.905 [101]	
$DyScO_3$	3.94 [100]	
$TbScO_3$	3.96 [100]	
$GdScO_3$	3.97 [100]	
$NdScO_3$	4.01 [100]	

As can be seen from table 2, anatase has a much smaller mismatch with respect to $LaAlO_3$(001) at −0.1% than it does with $SrTiO_3$(001) at +3.0%. With such a low lattice mismatch, it is not surprising that the anatase TiO_2(001) film becomes commensurate with the $LaAlO_3$(001) substrate [21, 22].

For the anatase TiO_2(001) film on $SrTiO_3$(001), Sugimura *et al* [23] showed that there is an expansion of the lattice to 3.81 Å for a 200 Å thick film [23]. So, while the film remains incommensurate, the lattice mismatch is relaxed. They also reported an accompanying compression to 9.4 Å in the c direction, out-of-plane from the surface.

In fact, Kennedy and Stampe show that there is a compression in the c direction for films grown both on $SrTiO_3$ and $LaAlO_3$ [22]. This is surprising for the $LaAlO_3$-supported film because there is already an in-plane compression, albeit a very small one. Figure 5 shows the lattice parameter in the c axis as a function of film thickness for the two films [22]. As one would expect, the compression of the film grown on $LaAlO_3$(001) is smaller (~9.48 Å for a 100 Å thick film) than for that grown on $SrTiO_3$(001) which is (~9.35 Å for a 100 Å thick film). For both cases the lattice parameter increases with film thickness. After a thickness of about 5000 Å, the film grown on $LaAlO_3$(001) has relaxed to a more-or-less pure anatase lattice spacing indicating the strain has been removed. On the other hand, the film grown on $SrTiO_3$(001) remained positively strained at ~9.6 Å from a thickness of 1000 Å at least up to 5000 Å.

Apgar and Martin [100] went further and formed anatase films on a series of different Ruddlesden-Popper/Perovskite oxide substrates with lattice parameters ranging from a = 3.71 Å for $YAlO_3$(110) to a = 4.01 Å for $NdScO_3$(110) which represents a mismatch from about −2 to +6%. By using the coincident-site lattice concept [102], they predicted that the preferred orientation for anatase should be (001) for lattice mismatches from −2 to +5%. Beyond +5%, the (100) face is preferred. To test this proposition, they formed TiO_2 films on all the substrates in table 2 except for $SrLaGaO_4$. XRD measurements indicated that anatase (001) was formed in each case

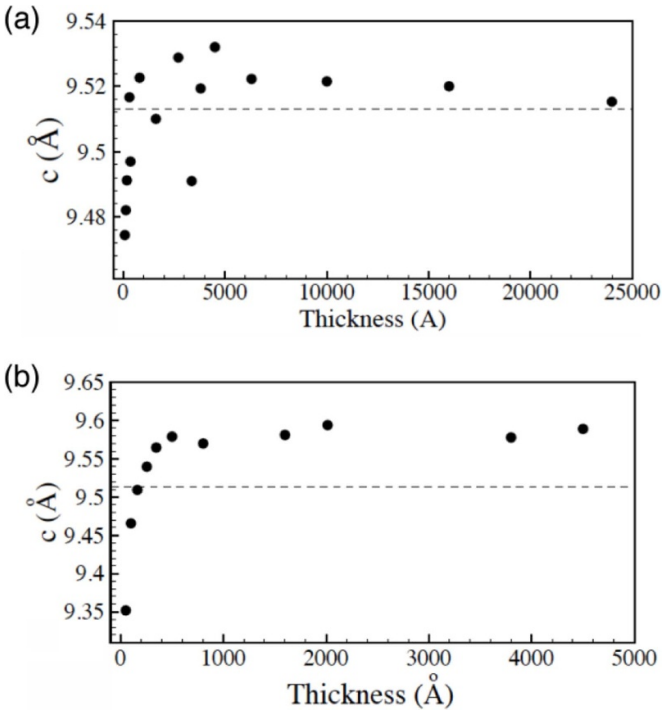

Figure 5. The thickness dependence of the out-of-plane lattice parameter, c, for anatase grown on (a) $LaAlO_3(001)$ and (b) $SrTiO_3(001)$. Reprinted from [22], Copyright (2003), with permission from Elsevier.

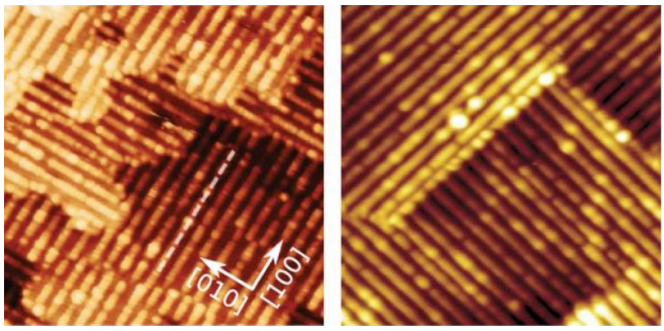

Figure 6. $(330\ Å)^2$ STM images of anatase (001)-(1×4). (a) The native surface. Reprinted figure with permission from [108], Copyright (2018) by the American Physical Society. (b) A film supported on $SrTiO_3(001)$. Reproduced from [28]. CC BY 3.0.

Table 3. Comparison of the surface energies of $TiO_2(001)$-(1×1) and with various models proposed for the anatase $TiO_2(001)$-(1×4) reconstruction as reported in [109].

Model	Surface energy ($J\ m^{-2}$)
(1×1)	0.90
MF	1.25
AMR	1.35
ADM	0.51

and that a mixture of (001) and (100) phases were present on $NdScO_3(110)$ which has a +5.9% misfit, consistent with their prediction. Previous work also shows that anatase (100) forms on MgO(100) which has $a = 4.21$ Å [103]. Depending on the growth conditions, rutile (110) is also found to coexist with the anatase film when MgO(100) is used as the support.

There are various implications for these differently-strained films. For instance, several calculations show that the straining of anatase can lead to a reduction in the band gap [49–51], crucial to the efficiency of TiO_2 as a photocatalyst [52–54]. By varying the substrate and the thickness of the anatase film, the effect on photocatalysis can be systematically investigated.

Indeed it has already been shown that an anatase film grown on $SrLaGaO_4(001)$ has a band gap 0.1 eV smaller than that grown on $LaAlO_3(001)$ and this was attributed to the tensile strain on the film grown on $SrLaGaO_4(001)$ [55].

It has also been shown that the film grown on $SrTiO_3(001)$ contains ~1% rutile [22]. This is thought to be because the large strain present on the anatase film on $SrTiO_3(001)$ causes a larger density of misfit dislocations which act as nucleation points for rutile growth. The ability to grow mixed anatase-rutile films may be important in photocatalysis due to several reports on a synergistic effect between anatase and rutile whereby the mixed phase is more active than pure anatase [104, 105], although this is disputed [106, 107].

Turning now to the detailed surface structure of anatase $TiO_2(001)$. It has been shown to undergo a (1×4) reconstruction both for single crystals and thin films. Due to the symmetry of the anatase (001) surface, two orthogonal domains [i.e. domains of (1×4) and (4×1)] can be seen as shown in the STM images in figure 6.

This reconstruction was first observed by Herman *et al* [26] who proposed a model with {103} microfacets (MF). This, however, proved inconsistent with STM studies reported by Liang *et al* [27] who instead proposed an added-and-missing row model (AMR). This model in turn compared rather poorly with simulated STM images and a third model was proposed which was described as an ad-molecule model (ADM) [109]. Not only does this model agree well with the simulated STM images, it was also by far the most stable of those tested, as shown in table 3. In fact, the table shows that MF and AMR are actually less stable than the unreconstructed (1×1) model.

Figure 7(a) shows the unreconstructed structure. It is terminated by a row of 2-fold O_b. To form the ADM model, every fourth row of O_b atoms are replaced with rows of TiO_3 units, which are also referred to as ridges.

To understand why the ADM is so stable, it is instructive to first examine the (1×1) structure. In the bulk-truncated model without relaxation, the two Ti–O bonds are equivalent, with lengths of 1.94 Å. Upon relaxation, one of these bonds is compressed to 1.76 Å while the other is elongated to 2.20 Å [109, 110]. Calculations show that the in-plane stress is significant for this unreconstructed surface and that this stress is significantly lowered in the ADM model where all the Ti–O bond now have lengths of ~1.8 Å. In fact the most recent calculations show that even in the ADM model, there remains a relatively large tensile stress in the [010] ridge direction [111]. This stress can be relieved by forming defects such as O vacs, interstitial Ti, and O adatoms. In doing so, the surface becomes

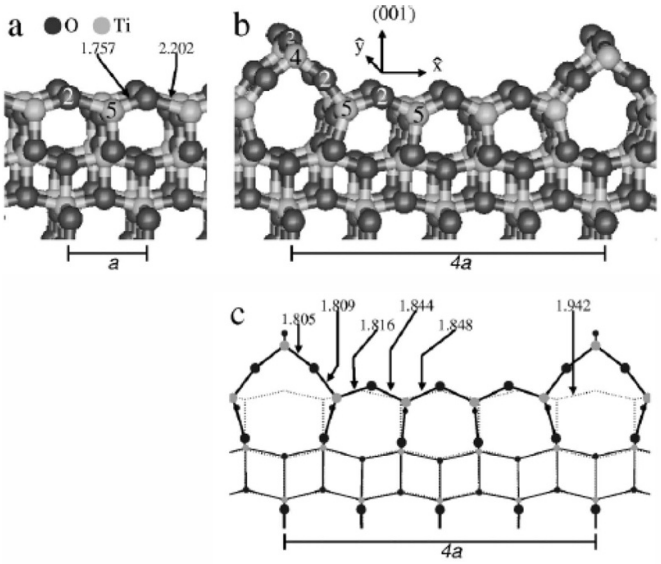

Figure 7. (a) Model of anatase TiO_2(001)-(1 × 1). (b) Relaxed structure of proposed ADM (1 × 4) reconstruction. The $\hat{x}$ and $\hat{y}$ axes correspond to the [100] and [010] directions, respectively. (c) Projection of the atomic positions of the ADM model. Dots with different sizes represent atoms belonging to different planes parallel to the figure. Dotted lines represent bonds in the ideal bulk-truncated surface. The lengths of some surface bonds are indicated in Å. The theoretical bulk in-plane lattice spacing, $a = 3.786$ Å is indicated. The coordination of some surface atoms are shown. Reprinted figure with permission from [109], Copyright (2001) by the American Physical Society.

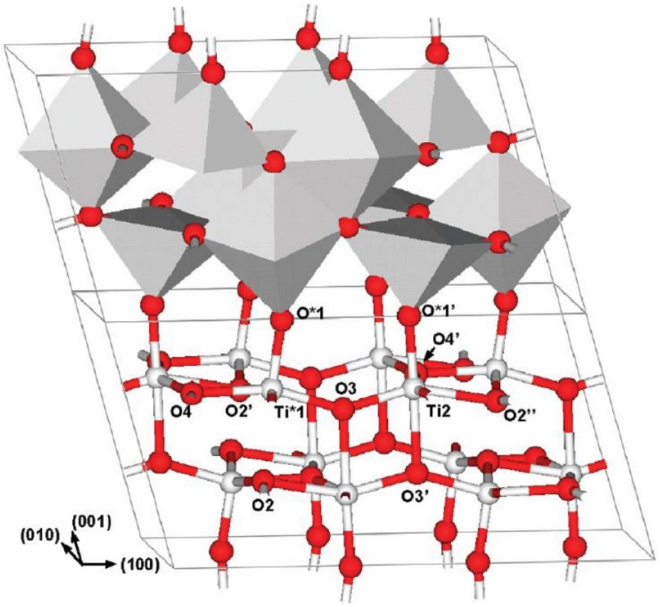

Figure 8. Computed equilibrium structure of bulk TiO_2(B). The grey lines mark the conventional monoclinic cell. Equivalent atoms are marked with a prime or a double prime. Two cells are shown, with polyhedral (top) and ball-and-stick (bottom) representations. Red balls denote O atoms and grey balls Ti. Reprinted with permission from [125]. Copyright (2009) American Chemical Society.

passivated. The implication is that this stress dictates the reactivity of the ADM structure and therefore to ensure that the surface is reactive, the surface must be free from defects. The calculations also show that the ADM structure becomes inert under 3% compressive lateral strain whereas a ~2% expansion to 3.905 Å (i.e. the $SrTiO_3$(001) lattice size) increases the reactivity [111].

While the ADM model has found a reasonable level of acceptance in the literature, due to contradictory observations about the reactivity of the surface to probe molecules such as water and methanol [28, 29, 108, 112] several other models have been proposed that are similar in construction to the ADM [28, 113–115]. These models also work by releasing the tensile stress supporting the importance of stress relief for this reconstruction regardless of the exact structure.

2.1.3. TiO_2(B). Compared to rutile, anatase, and brookite, TiO_2(B) is a much less well-known natural polymorph of TiO_2 named due to its close structural relationship with sodium titanium bronze [116]. First discovered and synthesised by Marchand *et al* [116] from the hydrolysis of $K_2Ti_4O_9$, the polymorph was subsequently confirmed to occur naturally as lamellae within anatase crystals [117].

TiO_2(B) is the least dense of the natural polymorphs of TiO_2 and is characterised by an open structure containing continuous channels which makes it an ideal host for intercalation. For this reason, there has been a resurgence of interest in TiO_2(B) in connection with energy storage materials, like Li-ion batteries [118, 119].

Study of the fundamental properties of TiO_2(B) are hampered by the lack of availability of single crystals. Recently, however, by using Pt(111), Pt(110)-(1 × 2), Au(111), Pd(100), and Pd(111) supports, TiO_2(B) thin films have been grown [32, 120–122] and this opens the way for reactivity studies [94, 95, 123].

TiO_2(B) has a monoclinic structure which is shown in figure 8. The conventional unit cell contains 8 TiO_2 units and from XRD, the lattice parameters are $a = 12.197$ Å, $b = 3.75$ Å, $c = 6.536$ Å, and $\beta = 107.16°$ [124].

The structure is usually described in terms of corner- and edge-sharing TiO_2 octahedra. However, the XRD data of Yahia *et al* [124] indicated that one of the Ti–O distances is longer than what would be expected from a single Ti–O bond (2.20–2.25 Å). Instead, they proposed a distorted square pyramidal environment for that Ti ion (denoted Ti^*1 in figure 8). This conclusion was supported both by their own calculations and those that followed [125].

The most stable face of TiO_2(B) is the (001) face which has two possible terminations denoted (001)-I and (001)-II by Vittadini *et al* [125] and shown in figure 9. The (001)-II termination was found to be quite unstable at 1.11 J m^{-2} on account of its unfavourable titanyl groups. On the other hand, the (001)-I termination is one of the most stable TiO_2 surfaces computed at 0.4 J m^{-2}. See for example table 3 for some anatase TiO_2(001) energies.

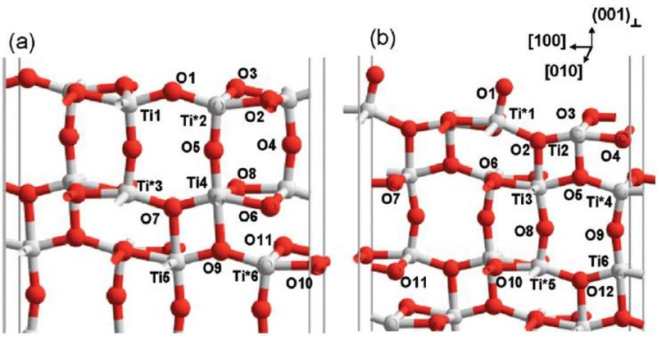

Figure 9. Structure of the relaxed TiO_2(B)-(001) surface with (a) type-I and (b) type-II terminations. (001)⊥ indicates the direction normal to the (001) surface. Reprinted with permission from [125]. Copyright (2009) American Chemical Society.

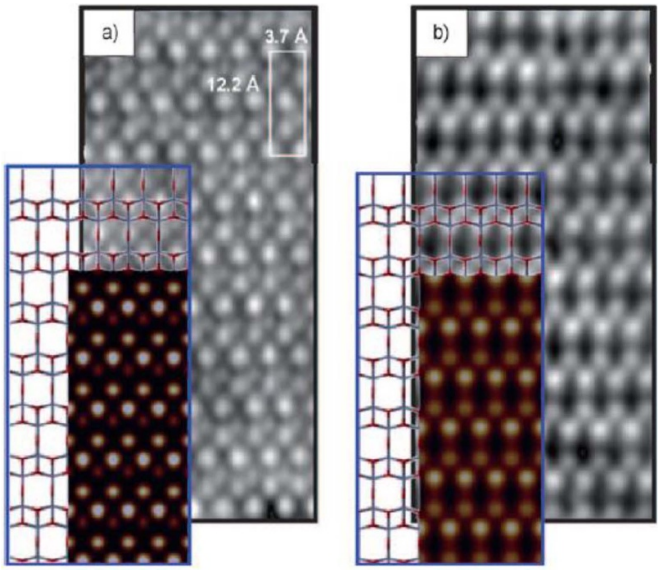

Figure 10. High-resolution (27 × 60 Å^2) STM images taken from the top of a *rect'*-TiO_2 island on Pt(111) with parameters (a) −0.7 V, 0.66 nA and (b) +0.7 V, 0.66 nA. The centred rectangular unit cell is outlined. The top view of the TiO_2(B)-(001)-I structure and the associated STM simulations are superimposed on part of the images. In the model, O is shown red and Ti blue. [121] John Wiley & Sons. Copyright © 1999-2020 John Wiley & Sons, Inc. All rights reserved.

The (001)-I face contains two Ti_5 ions, denoted Ti1 and Ti*2 in figure 9. These Ti ions are inequivalent: strictly-speaking only Ti1 carries dangling bonds because Ti*2 is already 5-fold coordinated in the bulk whereas this coordination is imposed on Ti1 by the bulk truncation.

A thin film of TiO_2(B) was first observed supported on Pt(111), where it was originally denoted as the *rect'* phase on account of its rectangular unit cell [126–128]. This *rect'* phase was found only at coverages higher than 2 monolayers (ML).

At lower coverages, another extremely stable phase is present which turns out to have a lepidocrocite-like structure [127] which will be discussed next in section 2.2.1.

When the coverage of the lepidocrocite-like layer is increased beyond 2 ML, it becomes unstable and transforms into the *rect'* phase which is stable in multilayers [127]. This is in line with calculations that show a 2 ML nanosheet of anatase (001) to be especially stable because it transforms into the lepidocrocite-like layer. Beyond 2 ML, frustrated lepidocrocite-like structures develop which are markedly less stable than the 2 ML lepidocrocite-like layer [129]. This drop in stability causes the phase transition to *rect'* beyond 2 ML.

Filled- and empty-states STM images are shown in figure 10 of the *rect'* phase [121]. The structure is represented by a centred, rectangular unit cell of 12.2 Å × 3.7 Å which is incommensurate with the substrate Pt(111). This unit cell is exactly matched to the TiO_2(B)-(001) unit cell (12.2 Å × 3.75 Å) within the error of the measurement and figure 10 also shows filled and empty states STM images together with the top view of the TiO_2(B)-(001)-I structure and the accompanying STM simulations. The simulated and experimental images match extremely well, even reproducing the different contrasts in the inequivalent Ti ions. It is worth noting that before this *rect'* phase was identified as a TiO_2(B) phase, a previous model was proposed [128] that consists of a pentacoordinated film derived from anatase TiO_2(101). This film is in fact almost identical to TiO_2(B)-(001)-I, the difference being that the two Ti_5 ions are equivalent in the pentacoordinated model [129].

Due to the 3-fold rotational symmetry of the substrate, three domains of TiO_2(B) can be observed in LEED, although by changing the deposition conditions, a full set of rotationally equivalent domains was also obtained, evident from bright circles in the LEED pattern [121].

The TiO_2(B)-(001)-I phase was also observed on Pt(110)-(1 × 2) with a = 12.0 Å being unstrained within the reported error and b compressed by 4.2% to 3.6 Å. In line with the reduced symmetry of this substrate, only two domains were observed, aligned ± 45º with respect to the Pt [001] direction. No other orientation of the film was observed [121].

The TiO_2(B)-(001)-I phase was also observed on Au(111) [120]. STM images in this case show the presence of a superstructure in addition to the motif already observed on the Pt substrates as shown in figure 11(a). This superstructure could be due to a Moiré-like interference pattern with the underlying substrate and/or a corrugation of the film. The unit cell matches that of TiO_2(B)-(001) exactly within the error of the LEED measurement.

Figure 11(b) shows a Ti L edge x-ray absorption spectrum (XAS) recorded from the Au(111)-supported TiO_2(B) film. It is plotted together with a spectrum from a TiO_2(B) powder sample as well as those from rutile and anatase. The spectrum from the TiO_2(B) film is almost identical with that taken from the TiO_2(B) powder giving strong evidence supporting the assignment of these films to TiO_2(B).

While the unit cell dimensions of these TiO_2(B) films indicate that there is no or very little overall strain, the presence of any substrate support means that different parts of the film are under different local strains. In the case of the film grown on Au(111), this strain may be manifested in the superstructure observed in STM [120].

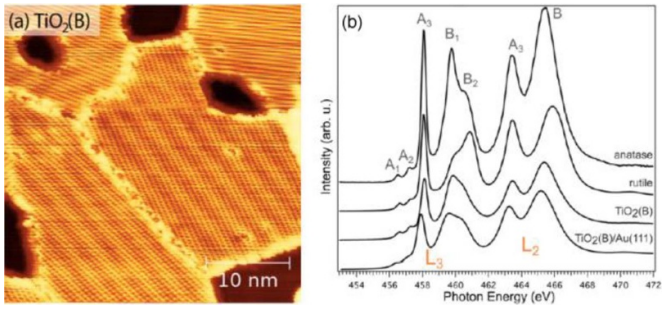

Figure 11. (a) STM image TiO_2(B)-(001)-I phase supported on Au(111). Reprinted with permission from [95]. Copyright (2015) American Chemical Society. (https://pubs.acs.org/doi/10.1021/acs.jpcc.5b00561) Further permissions related to the material excerpted should be directed to the ACS. (b) Ti L-edge XAS of the same surface plotted with rutile, anatase, and TiO_2(B) powder samples. Reprinted from [120], Copyright (2015), with permission from Elsevier.

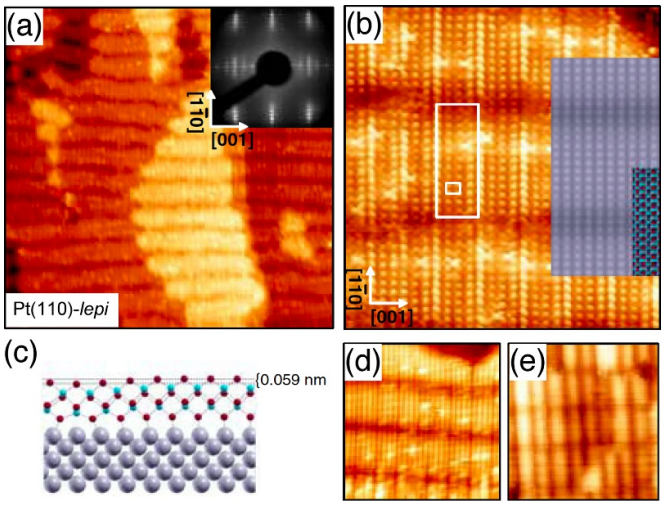

Figure 12. (a) Large area STM image (620 Å)^2 of a single-domain lepidocrocite nanosheet on Pt(110)-(1 × 2). Inset: (14 × 4) LEED pattern. (b) High resolution (137 Å)^2 STM image (0.28 V; 1.65 nA) of the nanosheet. The overlayer unit cell is indicated by the small rectangle and the superstructure by a large rectangle. Inset: Tersoff–Hamann STM simulation together with a ball model with O red and Ti blue. (c) Side view of the proposed model. High resolution STM images of the nanosheet with parameters (d) (136 Å)^2; 0.42 V; 0.9 nA) and (e) (180 Å)^2; 1.80 V; 1.0 nA. Reprinted figure with permission from [131], Copyright (2006) by the American Physical Society.

LEED measurements also suggest that the TiO_2(B)-(001) phase grows on Pd(100) and Pd(111) [122]. These films were more strained, with unit cells of 11.76 Å × 3.88 Å on Pd(100) and 11.7 Å × 3.6 Å on Pd(111). This corresponds to a compression of the TiO_2(B)-(001) film of 3.8% in *a* and an expansion of 3.4% in *b* on Pd(100) and a compression of 4.6% and 4.2% respectively for *a* and *b* on Pd(111).

2.2. *Thin films as novel structures*

Apart from thin films growing as mimics of native phases, novel phases may also grow. These novel phases sometimes grow because the strain that would otherwise be found in some other native-like structure makes it unfavourable. Within these novel phases, strain is also present due to interactions with the underlying substrate. Of particular interest is the question of whether these strained structures, or strained regions of the structure can provide preferential reaction sites so that the growth of, say, metal nanoparticles can be templated. This question will be addressed in section 2.3.

2.2.1. Lepidocrocite-like TiO_2. 2D inorganic crystals and nanosheets have received considerable attention recently due to the peculiar properties resulting from their sub-nanometre thickness. Specifically for TiO_2 nanosheets, their photocatalytic and semi-conducting properties are of interest. One successful strategy for forming such TiO_2 nanosheets involves delamination from layered lepidocrocite-like titanates [130].

Orzali *et al* [131] grew a 2D nanosheet-like layer on Pt(110)-(1 × 2) which they found to have a lepidocrocite-like (*lepi*) structure. The inset in figure 12(a) shows the LEED pattern of a 2 ML film which reveals the presence of a (14 × 4) supercell [131, 132]. This supercell can also be seen in the accompanying STM image in figure 12(a). The image is characterized by thick bright stripes and narrower dark stripes that run in the Pt[001] direction of the substrate. The average separation of the dark stripes is 39 Å along the Pt[1$\bar{1}$0] direction, which corresponds to 14 times the substrate periodicity (2.775 Å) in this direction. Deviations in this stripe separation account for their slightly wavy appearance. In high resolution STM images, for instance those in figures 12(b), (d) and (e), there is also a corrugation observable in the Pt[001] direction with a periodicity of 16 Å, four times the substrate periodicity (3.92 Å). As with the stripes, this ordering sometimes deviates so that ×3 and ×5 periodicities are frequently observed. The corrugation in this direction is highly dependent on the bias condition of the STM, clearly evident in the different appearances of (d) and (e).

While this describes the superlattice, the small unit cell dimensions of the overlayer can also be obtained as 3.0 Å × 3.9 Å from the atomically resolved image in figure 12(b). These lattice parameters are very close to those reported for lepidocrocite-like sheets, 3.0 Å × 3.8 Å in [130]. The structure of the bilayer can be imagined as a bilayer of anatase TiO_2(001) where the top layer is laterally shifted by half a unit cell along the [100] direction. In fact, when such a bilayer of anatase is modelled, it spontaneously relaxes to this *lepi* structure via a compression of the unit cell in the *b* direction as shown in figure 13. This *lepi* structure was computed to be only 0.16 eV per TiO_2 unit less stable than bulk anatase [129, 131].

The energy calculation indicates that the *lepi* structure is intrinsically stable and does not depend on some favourable interaction with the support. This is borne out to an extent by the appearance of this film on numerous surfaces with quite different characteristics: Pt(110)-(1 × 2) [131, 132], Ni(110) [74–76] Ag(100) [14, 133], W(100) [134], Pt(111) [126, 127], and Pt_3Ti(111) [135]. The unit cell parameters for

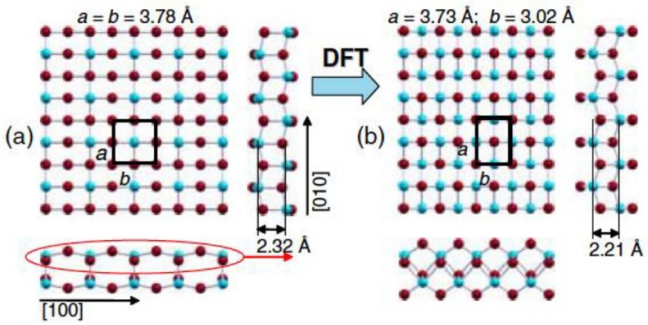

Figure 13. (a) Top and side views of an unsupported anatase (001) bilayer. (b) Top and side views of an unsupported lepidocrocite nanosheet, obtained from (a) by sliding the upper layer with respect to the lower one by half a unit cell along [100] as indicated by the ellipse in (a). O is shown red and Ti blue. Reprinted figure with permission from [131], Copyright (2006) by the American Physical Society.

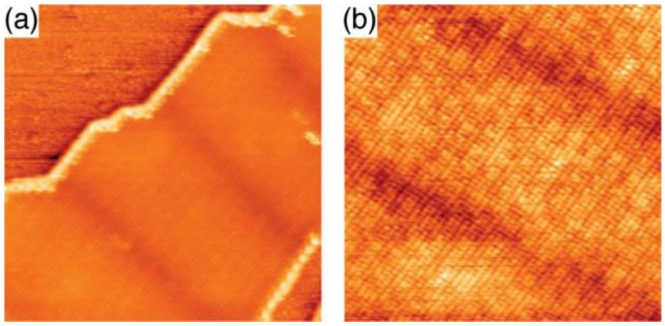

Figure 14. (a) 270 Å^2 and (b) (170 Å)^2 STM images of the *lepi* phase on Ag(100) showing the wide bright stripes and the narrow dark stripes. Reproduced from [133] with permission of The Royal Society of Chemistry, permission conveyed through Copyright Clearance Center Inc.

these substrates are shown in table 4 alongside the experimental dimensions of the free-standing lepidocrocite-like film [130], which numerous calculations closely match [129, 131, 133, 136]. On the square or rectangular substrates, either one or both side lattices of the *lepi* films are strained in order to form coincident lattices with the various substrates. These coincident relationships are also shown in table 4.

For instance for Pt(110)-(1 × 2), in the short *lepi* direction, 13 b_{lepi} units are matched with 14 b_{Pt} units, which involves a compression from the free-standing lepidocrocite lattice of ~0.4%. In the long *lepi* direction, there is a ~3% expansion of a_{lepi} in order to match a_{Pt}.

The *lepi* film on Ag(100) has an interesting structure [133]. In the long *lepi* direction (a_{lepi}), 4 *lepi* units are matched to 5 Ag units with a lattice compression of ~5%. In the orthogonal direction, there are wide bright stripes (90–110 Å) separated by narrower dark areas, as shown in figure 14. This was attributed to b_{lepi} not exactly matching b_{Ag} so that the more stable unstrained lattice is in the wider, bright stripes and the compressed lattice (2.89 Å) in the narrower, dark stripes. Due to the large compression required for the *lepi* film to be commensurate with Ni(110) in the long direction (8%) and the presence of similar bright and dark stripes [76], the same explanation probably applies for the *lepi* phase on Ni(110), i.e. some regions are commensurate and some are not.

As can be seen in table 4, *lepi* films can be created with strained lattices ranging from a 5% expansion to an 8% compression. On the other hand, due to the incompatible symmetry on the two hexagonal substrates, these *lepi* films are incommensurate and relatively unstrained. Thus these supported *lepi* films are a promising class of thin oxide film with which to test the effects of strain.

2.2.2. Polar TiO(1 + x) bilayers. Metal particles supported on oxide surfaces have long been studied due to their importance in heterogeneous catalysis [36, 37]. Apart from merely dispersing the metal particles, many oxide supports were found to play an active role, modifying the properties of the metal component. This was recognized as early as the 1970 s when Tauster and co-workers reported on strong metal-support interactions (SMSI) [137, 138]. SMSI can either promote or suppress reactivity. One of the most common ways that SMSI is manifested is by the encapsulation of the metal with a thin layer of the metal oxide which usually has the effect of passivating the metal.

This encapsulation has been quite well studied for model systems, such as metals supported on rutile TiO_2(110) [48, 139], For instance, encapsulation of Pt and Rh supported on TiO_2(110) by TiO_x upon annealing in UHV (>675 K) was observed as far back as the 1980s [140, 141]. Since then, evidence from ion scattering measurements clearly demonstrates that encapsulation occurs for Ni [142], Pd [143], Pt [144–146], Fe [147], and Rh [148].

Atomically-resolved STM images have been obtained for encapsulation layers grown on top of Pt [146, 149], Pd [35, 150], and Rh [34, 151–154], as well as Pd-Au bimetallic islands when the Au proportion is sufficiently low [35].

Figures 15(a) and (b) show STM images of the surface after the Pt/rutile TiO_2(110) system was annealed near to 1000 K [146]. Figures 15(c) and (d) show STM images of Pd/TiO_2(110)-(1 × 2) treated in a similar way [150]. In both cases, large, flat-topped hexagonal islands are formed with heights ~40 Å or higher and widths ~100 Å or greater. The hexagonal shapes of these metal islands suggest they are topped with metal (111) facets and this is corroborated in LEED [35, 144, 150] and reflection high-energy electron diffraction (RHEED) [143] measurements. A small minority of islands on the Pt/TiO_2(110) sample have a square shape but these will not be discussed further here. High resolution STM images taken from the tops of the hexagonal type A Pt islands reveal a zigzag structure as shown in figure 15(b). For Pd, a different type of zigzag structure was found as shown in figure 15(d). A pinwheel structure is also found in the Pd/TiO_2(110)-(1 × 2) system and this will be discussed later in section 2.2.2.2. For the Pd system, the same phases are found whether a TiO_2(110) (1 × 2) or (1 × 1) substrate is used [35, 150].

Ion scattering measurements show that the encapsulation layers are composed of Ti and O, both in the case of Pt [144–146] and Pd [143]. For Pt [145], grazing emission x-ray photoelectron spectroscopy (XPS) indicates that Ti^{2+} is

Table 4. Lattice constants of free lepidocrocite and various substrates together with the relevant coincident cells and expansions required to form the coincident cells.

	Geometry	a (Å)	Coincidence	Mismatch of a_{lepi} (%)	b (Å)	Coincidence	Mismatch of b_{lepi} (%)
Free-standing *lepi* [130]	Rectangular	3.8	—	—	3.00	—	—
Ag(100) [133]	Square	2.89	5Ag:4lepi	−5.2	2.89	Partial 1:1	−3.8
W(100) [134]	Square	3.16	7W:6lepi	−3.1	3.16	1:1	+5.1
Ni(110) [76]	Rectangular	3.52	Partial 1:1	−8.0	2.49	6Ni, 5lepi	−0.4
Pt(110) [131]	Rectangular	3.92	1:1	+3.1	2.775	14Pt:13lepi	−0.4
Pt_3Ti(111) [135]	Hexagonal	2.76	None	—		—	—
Pt(111) [127]	Hexagonal	2.77	None	—		—	—

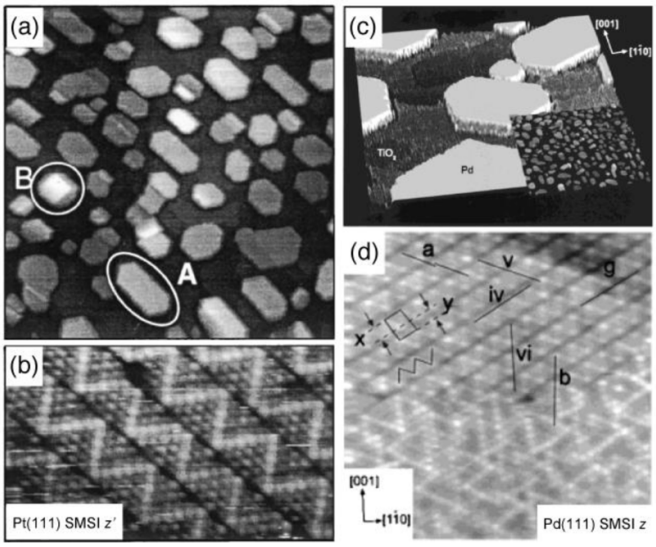

Figure 15. STM images of encapsulated nanoparticles formed by annealing Pt/TiO_2(110) and separately Pd/TiO_2(110)-(1 × 2) in UHV up to 970 K. (a) Large scale image of Pt(111) nanoparticles and (b) high resolution image taken from the top of a type A island showing zigzag rows (*z'*). Reprinted figure with permission from [146], Copyright (2000) by the American Physical Society. (c) Large scale image of Pd(111) nanoparticles and (b) high resolution image taken from the top of an island showing zigzag (*z*) rows co-existing with a disordered pinwheel structure. Reprinted with permission from [150]. Copyright (2002) American Chemical Society.

mainly present in the encapsulation layer whereas for Pd [150], Ti^{2+} and Ti^{3+} were found to be present. This suggests that for the Pt/TiO_2(110) sample, the encapsulating layer is TiO and for Pd, TiO_x ($1 \leqslant x \leqslant 1.5$).

Given that the Pd and Pt islands are relatively large and crystalline with (111) top facets, the encapsulation layer can be modelled theoretically by using single crystal (111) substrates [149]. More than that, by depositing Ti onto single crystal Pt(111) in a background of oxygen and further annealing in oxygen, Granozzi and co-workers systematically grew a series of TiO_x thin films [92, 128, 155–161], two of which are analogous to the zigzag structures found in the encapsulation layers. Similarly, several TiO_x thin films were recently observed on Pd(110), Pd(111), and Pt_3Ti(111), two of which are analogous to those found on the SMSI Pd(111) and SMSI Pt(111) systems [122, 135].

PhD measurements indicate that the stacking sequence should be Pt–Ti–O [92]. In fact, this stacking sequence applies to all of the reduced TiO_x phases reported in that work. DFT calculations by Jennison *et al* [149] also support this stacking sequence finding it to be more stable by 2.9 eV per TiO unit compared with when Ti is at the interface. The calculations further show that the Ti atoms are positively charged, although not ionic, and as a result the O atoms are negatively charged so that the surface is polar. Indeed, when Barcaro *et al* [158] modelled a free-standing TiO(111) bilayer, the Ti and O atoms mix into a single buckled layer in part to reduce this dipole moment.

While M–Ti–O (where M is the metal substrate) will not necessarily be the preferred stacking sequence for all metals, given the similar structures that arise, this stacking sequence does seem to apply to all the metals that will be discussed in this section. This sequence essentially arises from the stronger Ti–O bond compared to the M–O bonds in the metal substrates used.

2.2.2.1. Zigzag structures. The zigzag phases grown on Pt(111) [155, 158] and Pd(111) [122] shown in figure 16(a,b) are analogous to those found on the SMSI Pd(111) samples [35, 150]. These phases are denoted as *z*. In figure 16(a), the STM image shows clearly a structure that consists of bright stripes that are three atoms wide. For the SMSI Pd(111) *z* phase in figure 15(d), the central row of atoms is less clear and in the Pd(111) sample in figure 16(b), the central row is not visible. This is probably related to the tip condition because in other images of the *z* phase on SMSI Pd(111) and bimetallic Au-Pd(111), the central row can be seen more clearly [35]. The interatomic distance within the stripes measured by STM is about 3 Å. Between these stripes are narrow dark troughs. Guidelines in figures 15(d) and 16 show the zigzag motif where the zigzags are brighter. In all three images, a rectangular unit cell is marked out. The measured unit cell sizes are (8.6 Å × 6.8 Å), (8.7 Å × 6.5 Å), and (8.5 Å × 6.7 Å) on the Pt(111), SMSI Pd(111), and native Pd(111) samples, respectively. The reason why the lattice parameters of the *z* films are nearly identical regardless of the substrate is because it is incommensurate and thus only weakly coupled to the substrate.

The structure proposed for the *z* structure by Barcaro *et al* [158] is shown in figure 17. The model was derived from that proposed for a similar zigzag structure observed on VO_x/Pd(111) which had a V_6O_{14} structure [162]. However, due to the different chemistry of Ti and V, the model in figure

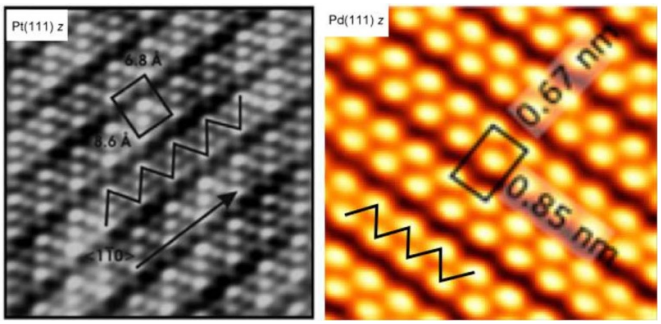

Figure 16. (a) (60 Å)^2 STM image of z-TiO_x grown on Pt(111). Reprinted with permission from [155]. Copyright (2005) American Chemical Society. (b) (43 Å)^2 STM image of z-TiO_x grown on Pd(111). Reprinted from [122], Copyright (2016), with permission from Elsevier.

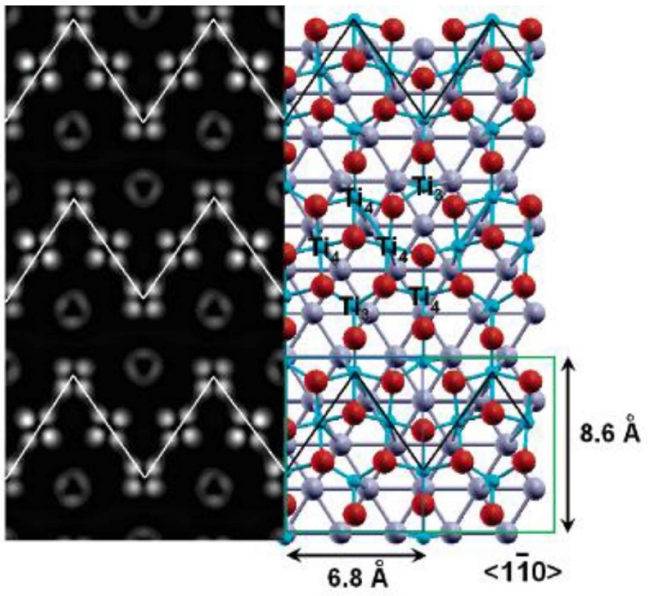

Figure 17. Model proposed for z-TiO_x on the basis of DFT calculations (right) and the corresponding simulated STM image at +1.00 V (left). The STM image is obtained by using four Pt layers to describe the metal support. The brighter 4-fold coordinated Ti atoms (denoted as Ti_4 in the figure) are responsible for the zigzag-like motif along the direction of the support, whereas the 3-fold coordinated Ti atoms (denoted as Ti_3 in the figure) are hardly visible. Only the outermost Pt layer is shown in the figure for clarity. Ti, O and Pt are shown as blue, red and grey balls, respectively. Reprinted with permission from [158]. Copyright (2007) American Chemical Society.

17 has a Ti_6O_8 structure which happens to match with the stoichiometry later reported by Ragazzon *et al* for the z phase on Pd(111) on the basis of XPS [122]. This stoichiometry is also consistent with the detection of Ti^{2+} and Ti^{3+} in the XPS for the SMSI Pd(111) sample [150]. As can be seen, the Ti species that comprise the zigzags are 4-fold coordinated with O (denoted T_4) and the Ti outside the zigzags are 3-fold coordinated with O (denoted T_3). In order to model incommensurate supported films with periodic DFT calculations, the substrate lattice must be artificially strained in order to match the dimensions of the film (or *vice versa*). From this calculation, an STM simulation was performed which matches the experimental images rather well: bright features are found on the zigzags that arise from the T_4 atoms, with the T_3 species being much dimmer. Dark troughs are also seen that arise from lines where O atoms bridge between Ti atoms. As the geometric height of the T_3 and T_4 species are within 0.1 Å of each other, the different contrast in STM arises from electronic effects. The interaction with the substrate was tested by nudging the structure by 1 Å along Pd[1$\bar{1}$0] and 1 Å in the orthogonal direction. The energy of the resulting film was essentially the same, confirming the weak interaction with the substrate.

The bright stripes of the zigzag structure shown in figures 15(b) and 18 are thicker than those of the z phase, being 4–6 atoms wide. This phase was denoted as z'. The interatomic distance within the stripes measured by STM is about 3 Å. The kinks in the zigzag have a mixture of V and W shapes. Whether the kinks are V or W shaped depends on the width of the stripes. When the stripes are 6 atoms wide, the kinks tend to be V shaped as seen in a few places in figures 18(c) and (d). When the stripes are 4 atoms wide, the kinks tend to be W shaped, as seen predominantly in figures 18(a) and (b). Finally, when the stripes are 5 atoms wide, they have a mixture of V and W, as seen in several places in figures 18(c) and (d). The bright stripes are separated by dark troughs which can be wide or thin. Close inspection of the wide troughs reveals the presence of circular defects and elliptical defects, marked by dotted circles and ellipses in figures 18(a) and (b), respectively.

Notice that the unit cell stays the same size regardless of the number of atoms in the bright stripes. This is because the

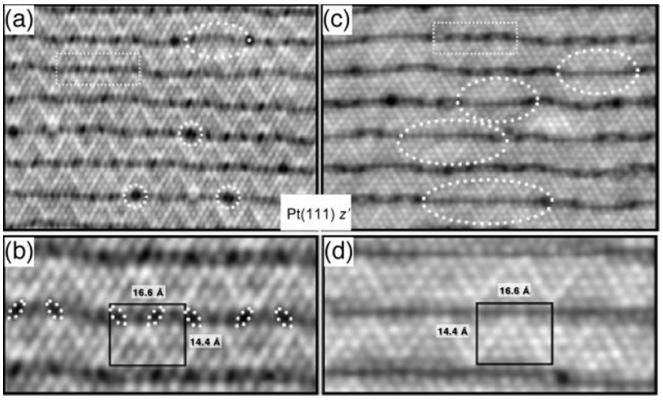

Figure 18. STM images of the z'-TiO_x thin film. (a) 140 × 100 Å^2 image following 30 min annealing at 673 K and (b) a magnified region of (a) where wide troughs are abundant (65 × 33 Å^2). (c) 150 × 100 Å^2 image after 110 min annealing at 673 K and (d) a magnified region of (c) where thin troughs are abundant. The dotted rectangles in (a) and (c) outline wide troughs and the dotted ellipses outline regions where thin troughs are evident, more abundant after prolonged annealing. The small dotted ellipses in (b) outline quasi-periodic defects within the wide troughs. The unit cells are also outlined in (b) and (d). Reprinted figure with permission from [163], Copyright (2008) by the American Physical Society.

wider bright stripes are correlated with thin troughs and the narrower stripes are correlated with wide troughs. In fact, the thickness of the stripe can change along its length, which leads

to the meandering appearance. This also points to a common basic structure regardless of the width of the stripes.

By following the stacking order already established, i.e. Pt–Ti–O, a model was gradually built for the *z'* structure as follows [163]. If the lattice parameter of TiO(111) was the same as Pt(111), then Ti atoms could be placed in Pt threefold hollow sites and likewise, the top layer of O could be placed in Ti hollow sites. This does not happen for two reasons: (1) the lattice strain is too high [~3 Å for a TiO(111) layer *vs.* 2.775 Å for Pt(111)] and (2) the preferred stoichiometry is higher. Instead, Ti fills the Pt(111) hollow sites in triangles or (pseudo-triangles) separated by dislocation lines. Across the dislocation lines, the stacking switches between fcc and hcp hollows. Within the triangles, the Ti atoms are 3-fold coordinated to O and along the dislocations, they are 4-fold coordinated to O thus also solving the stoichiometry issue [164].

The proposed models for four atom-wide bright stripes are shown in figure 19. In figure 19(a), two bright stripes are coupled with Ti_2O_3 units that sit in the wide trough giving a stoichiometry of $TiO_{1.25}$. As can be seen from the simulated STM image, the key features of the experimental image are well reproduced. The zigzags (or T_4) atoms appear brighter, the trough appears dark, and the elliptical defects are present. The model in figure 19(b) is the same except for a rearrangement of the Ti and O atoms in the trough. The simulated STM image of this second model is essentially the same, the difference being that round defects can be seen in the trough rather than the elliptical defects. Finally adding a further Ti atom at the apex of the W kinks leads to the model in figure 19(c) which reproduces the V-shaped kink and gives a stoichiometry of $TiO_{1.2}$. The trough is now filled and appears in the simulated image as a thin trough. By the same token, the bright stripe is now 5 atoms wide. Within the accuracy of the calculation, these structures are practically isoenergetic.

There are important similarities and differences between the z and z' structures. Both models solve the lattice mismatch problem with the creation of denser Ti stripes separated by less dense troughs. At the same time, the issue of crowding in the O layer is solved by having dislocations within the stripes, i.e. at the zigzags. The key difference between the structures is that while both have less densely-packed troughs, in the case of z', the bare metal substrate is actually exposed in so-called pico-holes. This has consequences for the film reactivity as we shall see in section 2.3.

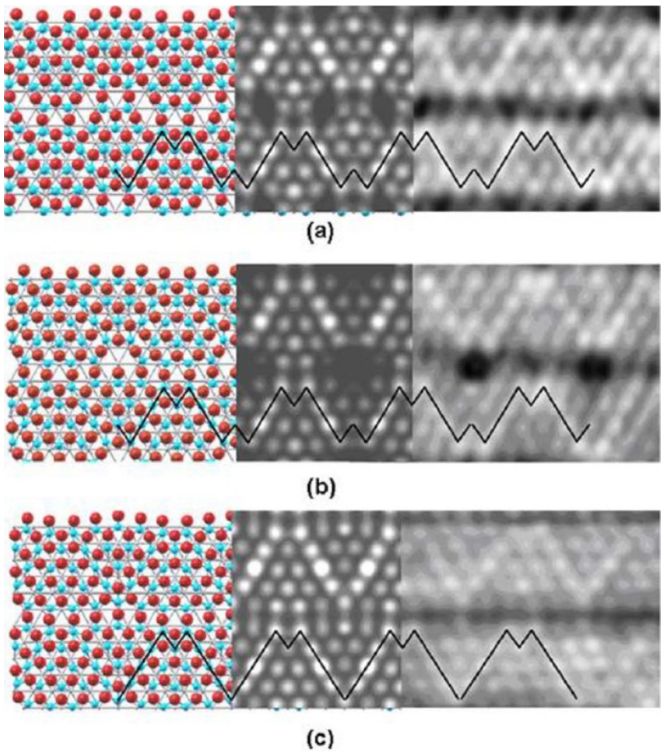

Figure 19. Comparison between the simulated and experimental STM images for the z'-TiO_x structure for different models that account for slightly different structures seen in STM. (a) and (b) have $TiO_{1.25}$ stoichiometry whereas (c) has $TiO_{1.20}$ stoichiometry. In the ball and stick models, O is red and Ti is blue. Reprinted figure with permission from [163], Copyright (2008) by the American Physical Society.

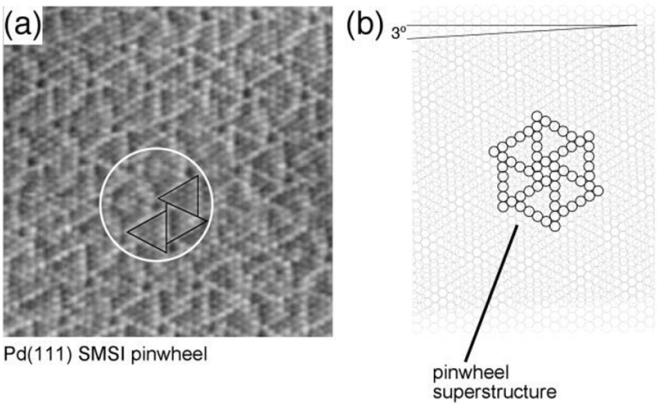

Figure 20. (a) $(105\ Å)^2$ STM image of the pinwheel structure formed by annealing $Pd/TiO_2(110)$-(1×2) in UHV up to 970 K. The circle highlights a pinwheel and the three triangles mark out part of the ideal pinwheel structure. (b) A hexagonal lattice of 3.25 Å periodicity is rotated by 3° and superimposed on a lattice of 2.75 Å periodicity giving rise to the superstructure drawn in bold. This pattern reproduces the pinwheel motif seen in (a). Reprinted with permission from [150]. Copyright (2002) American Chemical Society.

2.2.2.2. Wheel structures. An image of the pinwheel structure arising from encapsulation of Pd(111) on rutile $TiO_2(110)$-(1×2) is shown in figure 20(a) [150]. The structure can be described by six interlocking triangles that rotate around a dark central hub where the triangle perimeters are brighter. The general structure can be simulated by superimposing an expanded, rotated hexagonal lattice over the Pd(111) substrate lattice as shown in figure 20(b). The resulting picture in figure 20(b) forms a Moiré interference pattern that strongly resembles the STM image. As such, it was concluded that some TiO_x layer grows on the Pd(111) islands with a lattice separation of 3.25 Å rotated by $\pm$ 3° with respect to the Pd(111), consistent with the observations from LEED.

Table 5. Lattice constants of substrates and wheel overlayers together with the rotation angle between the substrate and overlayer lattices. The overlayers are pinwheels for Pd, Rh, and Au. For Pt, the type of wheel structure is indicated in the table.

Substrate	$a_{substrate}$ (Å)	a_{wheel} (Å)	Angle (°)
Rh(111) [34]	2.69	3.2	1.8
Pd(111) [150]	2.75	3.25	3
Pt(111) *w* [155]	2.775	3.26	1.36
Pt(111) *w′* [155]	2.775	3.18	3.5
Pt(111) w_{int} [156]	2.775	3.23	3.3
Au(111) [165]	2.89	3.27	1.68
Au(111) [33]	2.89	3.20	1.7

Very similar pinwheel structures have also been formed by encapsulating TiO_x layers on Rh [34, 151–154] and Pd-Au bimetallic [35] nanoparticles grown on TiO_2(110), as well as by the deposition and subsequent oxidation of Ti on Au(111) [33, 165]. All these structures are characterized by six interlocking triangles that rotate around a dark central hub, their appearance only differing in the size of the interlocking triangles. The lattice parameter of these TiO_x films ranges from about 3.2 to 3.27 Å, almost the same as observed on Pd(111) which points to the same structure in the film. Three other wheel structures (named *w*, *w′*, and w_{int}) have also been observed for TiO_x grown on Pt(111) [92, 126, 155, 156, 159]. While these structures have a different appearance in STM images compared to the pinwheels, the films have been shown to be essentially the same: a TiO_x layer supported on the metal substrate rotated slightly as shown in table 5.

These TiO_x layers have a mean lattice separation of 3.23 Å with a range of just ±0.05 Å or ±1.5%. So rather than introducing very large strains by compressing the TiO_x lattice by significant values of 11%–19%, the mismatch is accommodated by the small angle rotation.

As discussed in section 2.2.2.1, the stacking sequence for these films is M–Ti–O [92, 149]. As such, most models proposed for these structures are based on a hexagonal Ti layer that sits in the interface between the substrate and oxygen layers. Due to the lattice mismatch, the Ti atoms occupy a range of different M(111) sites: atop, quasi-atop, bridge, quasi-bridge, threefold, and quasi-threefold hollow. On top of the Ti layer, O atoms then occupy the Ti hollow sites. This means that the Ti are 3-fold coordinated (denoted T_3 here) with O and the stoichiometry is TiO. In these models, the Ti at the central hubs are in purely atop positions and are therefore at least tentatively proposed to be missing, bringing the stoichiometry to slightly above TiO [33, 150, 156].

However, in a recent DFT calculation by Mutombo *et al* [34], a different model was proposed. Their work followed the building principles employed by Sedona *et al* [163] for the *z′* structure and developed further for metal oxide films in general by Barcaro *et al* [64, 164]. In the model of Mutombo *et al* [34], Ti is initially placed only in Rh(111) 3-fold hollow sites as shown in figure 21(a). However, because of the lattice mismatch, this leads to dislocations. These dislocations separate triangles with fcc occupation from triangles with hcp occupation just as in the model for the *z′* structure [163]. The Ti at these dislocations relax into bridge positions and are 4-fold coordinated (T_4) with O whereas the Ti within the triangles are 3-fold coordinated (T_3) with O [figure 21(b)]. STM simulations show that these T_4 atoms appear brighter and form the spokes in the pinwheel structures.

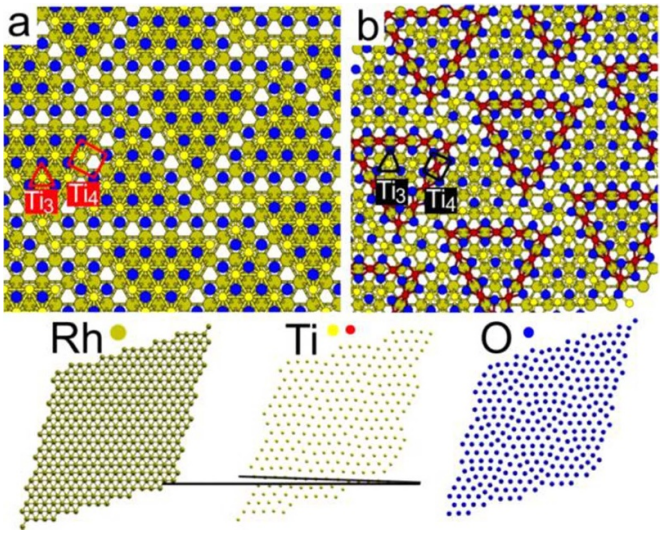

Figure 21. (a) Initial and (b) relaxed atomic positions of the TiO_x film. In (a) Ti is placed exclusively in 3-fold Rh hollow sites. The Ti is arranged in T_3 triangles with fcc occupation and T_3 triangles with hcp occupation where these are separated by dislocations of T_4. In (b), the T_4 atoms relax into bridge positions. At the bottom of the figure the relaxed atomic layer structure of the different elements (Rh, Ti, O) can be seen. Reprinted with permission from [34]. Copyright (2016) American Chemical Society.

2.2.2.3. Kagomé-like structure. Figure 22 shows an STM image of another film that has a quite distinctive appearance. The image is characterized by a patched overlayer with an open hexagonal motif, the latter appearing more clearly in the high resolution image in figure 22(b). The hexagonal motif has a periodicity of about 6 Å and is incommensurate with the substrate as also evident from the 2.15 × 2.15 LEED pattern.

Rather than edge-sharing as in a honeycomb arrangement, the hexagons are connected via their vertices, so that triangles are created at these connections. Such a structure is often referred to as a kagomé lattice, named after Japanese woven baskets with the same structure but in the macroscale [166]. As such, Sedona *et al* [155] name this a kagomé-like nanolayer (*k*-TiO_x).

In the most ordered regions, the patches have a period of ~35 Å [160]. By superimposing this *k*-TiO_x lattice that has a 6 Å lattice parameter onto the substrate Pt(111), it can be seen that 6 unit cells of *k*-TiO_x coincide with 13 Pt(111) cells giving the superstructure periodicity of 36 Å. This matches well with the size of the patches and indicates that the patchwork appearance arises from a Moiré-like interference.

In line with the other reduced TiO_x phases in this section, a model was built with a Ti–O bilayer with Ti at the interface as shown in figure 22(c). As can be seen, the stoichiometry of the structure is Ti_2O_3. In common with the incommensurate

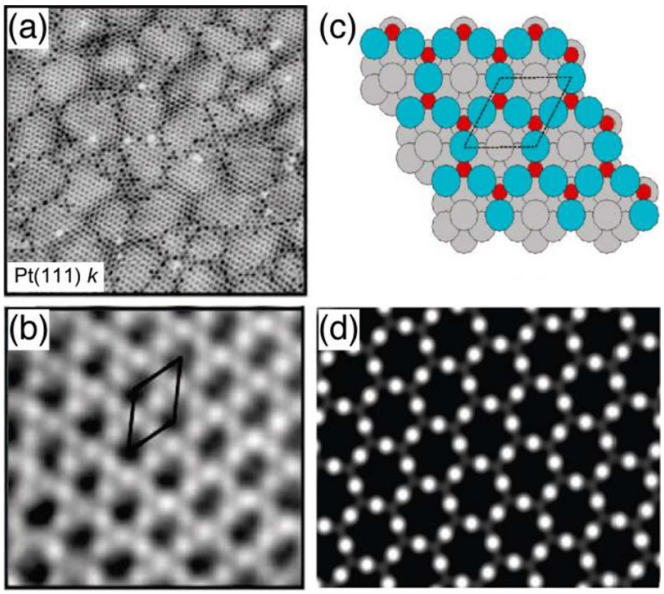

Figure 22. *K*-TiO_x on Pt(111). STM images with parameters (a) (300 Å)^2, 1 V, 1.0 nA and (b) (30 Å)^2, −0.4 V, 1.06 nA. (c) Proposed structural model and (d) simulated STM image at −0.4 V. In (c) Ti is shown red and O blue. Reprinted with permission from [160]. Copyright (2009) American Chemical Society.

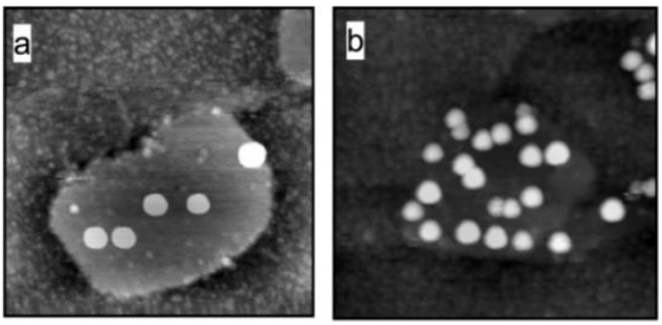

Figure 23. (820 Å)^2 STM images of the TiO_2(B)-(001)-I/*k*-TiO_x system after the deposition of (a) 0.2 ML and (b) 0.8 ML Au. Reprinted with permission from [128]. Copyright (2008) American Chemical Society.

z phase, a strained Pt(111) surface was used as a substrate in order to make the periodic DFT calculations tractable. STM simulations using this model agree well with experimental images as shown in figure 22(d) [160].

Sedona *et al* [155] make note of an almost identical-looking TiO_x film found supported on Ru(0001) [167]. A Moiré-like superstructure was also observed with a 28.5 Å periodicity and this film likely has the same origin as the *k* phase. Likewise, Wu *et al* [165] observed a similar structure supported on Au(111) and propose the same model further supported by their Auger electron spectra which is consistent with Ti_2O_3 stoichiometry. However in the case of Au(111), the Ti_2O_3 lattice is commensurate with the substrate and forms a (2 × 2) overlayer. If we assume the preferred spacing of the lattice is 6 Å (i.e. that found on the incommensurate substrate), then this lattice is compressed by 3.8%. Notice that Wu *et al* [165] observe an edge-sharing honeycomb motif in their STM images as do other workers who observed the same structure on Au(111) [31]. This presumably arises simply from the STM imaging Ti states rather than O states in figure 22. As such, this phase tends to be referred to as a honeycomb (*hc*) phase when supported on Au(111).

Interestingly, this *k* or *hc* lattice can be thought of as a single nanosheet with an ordered array of pico-holes, which as we will see in section 2.3 has implications for its reactivity.

2.3. Thin film reactivity

The reactivity of these TiO_x films has received considerable attention in the literature. For novel, or otherwise difficult to prepare samples, it is important to understand their fundamental properties. For those films with large-scale ordered defects and/or strain-relief structures, there is considerable interest in exploiting this property to template ordered adsorption of other materials in order to build up nanodevices.

In this section, several reactivity studies are included because they take place on the strained films or films that may have some local strain such as the TiO_2(B) films supported on Pt and Au. This does not mean that all the observations are a consequence of that strain.

2.3.1. Gold nanoparticles. The Au/TiO_2 system is a particularly well-studied system, partly because of the work by Hutchings [168, 169] and Haruta *et al* [170, 171] in the mid 80s which showed the enhanced activity of nanosized Au. This provides the motivation for the many studies of the interaction of Au with these TiO_x films.

Sedona *et al* [128] compared the reactivity of the *k*-Ti_2O_3 and TiO_2(B)-(001)-I films. They were able to form a surface with both phases present and this allowed both films to be under exactly the same Au dosing conditions. Figure 23 shows an STM image of the surface following deposition of 0.2 ML [figure 23(a)] then 0.8 ML [figure 23(b)] Au. A TiO_2(B) island is in the centre of the images and it contains large Au nanoparticles. This island is surrounded by the *k*-Ti_2O_3 layer on which much smaller Au nanoparticles are present. These results were rationalized via DFT calculations. On the TiO_2(B) film, the most stable site for an Au atom was found above an oxygen with an adsorption energy (E_{ads}) of only 0.30 eV. Diffusion barriers to neighbouring O species were also found to be very low at 0.05 and 0.06 eV, depending on the route. This means Au atoms are extremely mobile on this surface and the Au is able to agglomerate into large nanoparticles.

In stark contrast to this, Au atoms penetrate into the pico-holes of the *k* film and are strongly adsorbed with $E_{ads} = 2.96$ eV. The activation energy for the Au atom to jump out of the hole is 2.4 eV. This means that while the Au can hop easily among the O atoms, they are trapped once they find the holes (or other Au species pinned at the holes). This explains why larger nanoparticles do not form on the *k* film.

These results are summarized in table 6 where the TiO_x phases are arranged in approximate order of reactivity. Apart from the present case, the dosing conditions and computational

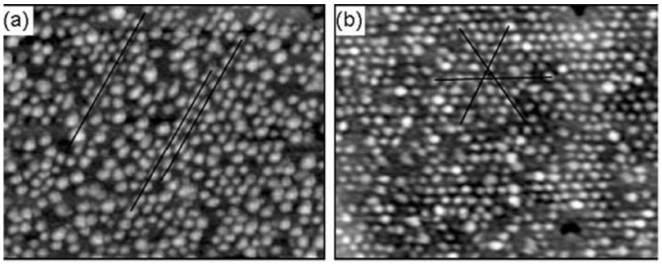

Figure 24. (500 × 400 Å^2) STM images of Au nanoparticles (0.35 ML) on the z'-TiO_x phase. (a) As-deposited at 300. (b) After post-deposition annealing in UHV at 600 K for 15 min. Reprinted with permission from [161]. Copyright (2009) American Chemical Society.

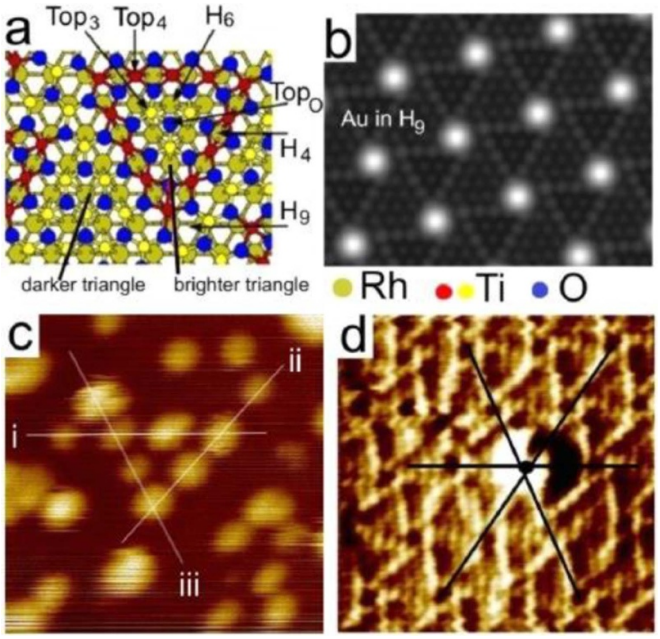

Figure 25. (a) Adsorption sites for Au atom used in the DFT calculations. (b) STM simulation of Au adsorbed at the H9 site. (c) (100 Å)^2 STM image after < 0.005 ML Au was deposited on the pinwheel at 300 K. (d) (70)^2 STM image showing the position of an Au nanoparticle consisting of six to eight Au atoms relative to the wheel structure. Reprinted with permission from [34]. Copyright (2016) American Chemical Society.

methods are different so small differences in reactivity may not be definitive.

The clearest difference between k-Ti_2O_3 and TiO_2(B) is the presence of pico-holes for the k phase and that is considered to be the decisive factor.

A general rule of thumb that the pico-holes determine the reactivity of the film seems to hold quite well. The z' phase has a series of pico-holes in the troughs and when Au is deposited onto the surface and gently annealed, the small Au nanoparticles align in rows along these troughs, as shown in figure 24(a) [159]. On the other hand, the *w'* phase has no evidence of ordered defects or pico-holes and deposition of Au leads to the growth of large nanoparticles [159, 161] in a similar way to the TiO_2(B) phase. Sedona *et al* suggest that the different growth behaviour of Au between the z' and w' phases is due to the pico-holes in the z' troughs acting as the nucleation sites which gives rise to the templated growth of Au [159].

This suggestion was borne out by DFT calculations that showed the pico-hole had an adhesion energy (E_{adh}) of 1.70 eV compared with E_{ads} of ~0.8–1.0 eV at the Ti sites [172]. The reason for the smaller interaction energy of Au with the z' phase compared with that on k-Ti_2O_3 is because the smaller size of the pico-hole in the z' structure presents a steric hindrance. This steric effect is also evident from the fact that the Pt–Au interaction in the pico-hole is actually weaker than it is with the equivalent site in pure Pt(111) where E_{ad} was calculated at 2.42 eV. Furthermore, when a smaller metal, Pd, was modelled E_{adh} was much higher at 3.11 eV because the Pd could penetrate more easily into the Pt(111) underneath. In this case, the Pd–Pt interaction was increased in the pico-hole relative to that on pure Pt(111) where is was only 2.73 eV.

While the z phase shares many features with the z' phase, there are no pico-holes on the z phase and the expectation is that there will be no templating effect. As expected, STM taken from Au deposited on the z phase of an encapsulated Au-Pd(111) nanoparticle with Au:Pd in a 1:5 ratio [35] showed no evidence of any preferential nucleation. The most stable sites calculated for Au adsorption on the z phase are the Ti sites which have E_{ads} of 1.1–1.6 eV [172].

The pinwheel structures grown on Rh(111) and Au-Pd(111) are structurally almost identical to the *w'* phase as we saw in section 2.2.2.2. The key differences were the bright perimeters of the triangles and the dark central hub. When Au is deposited on these pinwheel structures, STM images reveal that Au nanoparticles grow initially as one atom thick 2D nanoparticles with a degree of large-scale periodicity, very close to the periodicity of the pinwheel structure [34, 35]. This is diagnostic of substrate-templated adsorption. DFT calculations on the Rh(111)-supported pinwheel show that the most stable adsorption sites for Au is adjacent to the T_4 atoms at the corners of the triangle, i.e. at or near the central hub as shown in figures 25(a) and (b).

As discussed earlier, it has been speculated that the dark central hub arises from a missing Ti (i.e. a pico-hole) [33, 150, 156]. However, the calculations of Mutombo *et al* [34] suggest instead that the dark hub simply results from a local downward relaxation of the film. Thus it appears that the lattice strain causes these sites to be favoured for Au adsorption [34, 35]. Interestingly, the stabilization here is virtually as strong as that from the sterically-unhindered pico-holes of the k phase with a value of $E_{ad} = 2.72$ eV. It would be interesting to see if this templating effect was common among the other wheel structures that also contain this dark central hub.

While, we have seen that TiO_x structures can template the growth of a regular arrangement of nanoparticles, the metal particles can also affect the stability of the TiO_x nanophase. Sedona *et al* [159] found that when they annealed the ordered overlayer of Au nanoparticles on the z' phase to ~600 K, there was a shift to a hexagonal arrangement of the Au nanoparticles without any change in the Au particle size as shown in figure 24. With the help of DFT calculations, Bacaro *et al* [161] show

Table 6. Experimentally determined widths, heights, coverages, and preferential nucleation sites of Au nanoparticles supported on several TiO_x films together with their DFT calculated energies where available.

Phase	Width (Å)	Height (Å)	Coverage (ML)	Energy (eV)	Preferential nucleation sites
k [128]	15–20	2	0.2	2.96	Pico-holes
k [128]	25	2.5	0.8	2.96	Pico-holes
Rh(111) pinwheel [34]	15–20	2	0.1	2.72	Hub
Pd:Au(111) pinwheel [35]	23	1.1	0.1	—	Hub
z' [159]	13	2 or 4[a]	2	1.70[b] [172]	Pico-holes
w' [159]	34	15	2	—	None
TiO_2(B)[c] [128]	50–60	15	0.2	0.30	None
TiO_2(B) [128]	50–60	15	0.8	0.30	None

aTwo values are given because there is a bimodal distribution.
[b]This value corresponds to the adhesion energy whereas all other values correspond to adsorption energies.
[c]The calculation was based on the pentacoordinated model which is almost identical to the TiO_2(B) model but with the two Ti_5 ions being identical. This does not affect the conclusions.

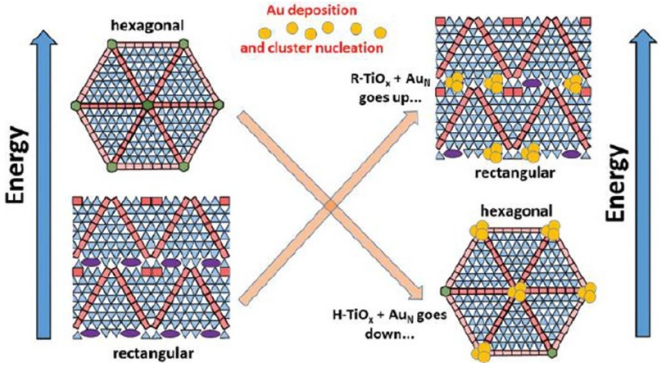

Figure 26. Schematic diagram showing the energy crossing between the z' phase and the hexagonal analogue induced by deposition and annealing. The metallic Au nanoparticles are pinned at the pico-holes exposing the underlying metal substrate. Triangles and rectangles represent TiO_3 and TiO_4 units, respectively, while hexagons and ellipses indicate hexagonal and rectangular pico-holes, respectively. Reproduced from [64] with permission of The Royal Society of Chemistry, permission conveyed through Copyright Clearance Center Inc.

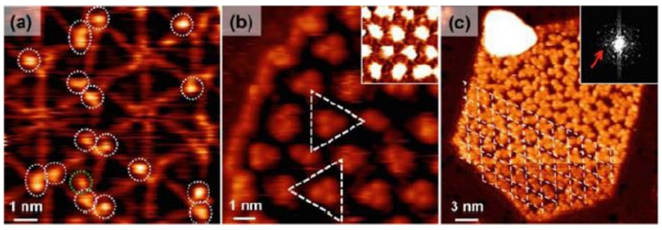

Figure 27. Adsorption geometry of TMA at different coverages. (a) 0.02 Ml. TMA groups (white circles) appear as bright protrusions. The green circle marks a rare TMA group adsorbed at the centre of a triangle. (b) 0.06 ML. Triangles mark two equivalent 3-fold symmetries. The inset shows a section of the image with high contrast that reveals the pinwheel structure of the underlying film. (c) 0.15 ML. A grid constructed with a 28 Å periodicity is drawn to show the long-range periodicity of the TMA. The inset shows the fast Fourier transform of the image. The clear hexagonal pattern, corresponding to the pinwheel periodicity, is marked by a red arrow. Reprinted with permission from [33]. Copyright (2014) American Chemical Society.

that the underlying TiO_x surface undergoes a phase transition to a hexagonal analogue of the z' structure as shown in figure 26. This hexagonal phase is normally less stable than the z' phase but upon adsorption of Au nanoparticles, the situation is reversed because the pico-holes in the hexagonal phase are larger and better able to accommodate the Au nanoparticles. Similar adsorbate-induced phase transitions were observed for Fe nanoparticles on the z' phase as well as redox reactions whereby the Fe is oxidised by the film [173, 174].

2.3.2. Trimethyl acetic acid. Apart from templating of metal nanoparticles, it is also of wide interest to assemble ordered arrays of organic molecules. Like Au nanoparticles, carboxylic acids have also been widely used to probe the reactivity of different TiO_x samples [175, 176] and trimethyl acetic acid (TMAA) has been particularly well studied in recent years, with significant attention given to its photoreactivity [177, 178]. Li *et al* [33] used this molecule to probe the reactivity of the pinwheel grown on Au(111). As with Au in the studies by Mutombo *et al* [34] and Gubó *et al* [35], here the hub or rather the Ti atoms near the hub are found to be particularly reactive.

Figure 27 shows an STM image of the Au(111)-pinwheel surface after deposition of increasing amounts of TMAA [33]. Figure 27(a) shows the lowest coverage (0.02 ML). Bright spots attributed to dissociated trimethyl acetate (TMA) are seen adjacent to the hubs. At the slightly higher coverage (0.06 ML) shown in figure 27(b), clusters of three TMA species are seen with a large-scale periodicity. This periodicity matches that of the pinwheel and in the highly-contrasted image in the inset, the triad of TMA can be seen to be centred about the hubs. At the higher coverage of 0.15 ML shown in figure 27(c), the templating is less obvious. Nevertheless, the Fourier transform of the image shown in the inset reveals the hexagonal ordering caused by the templated growth.

The model proposed by Li *et al* [33] for the pinwheel structure is based only on the Moiré interference model. A hexagonal Ti lattice is placed on top of the Au(111) lattice and rotated by 1.7° creating a pinwheel with spokes and a central hub. The dark hub corresponds to missing Ti atoms that otherwise would be located directly above Au atom. The

Ti atoms around the hub are in quasi-atop positions and as we move towards the centre of the triangles, these Ti atoms gradually shift towards threefold hollow sites, with the spokes occupying bridge and quasi-bridge sites. The O atoms in the top layer occupy threefold hollow Ti sites.

On the basis of this model, Li *et al* attribute the enhanced activity to the strain in the system that leads to a smaller Ti–O separation near the central hubs. This smaller Ti–O separation has two effects: (i) it makes the Ti more accessible to TMA and (ii) after adsorption, the TMA has a dipole pointing towards the surface and is repelled by the dipole of the film. The dipole of the film is smallest near the hub and so offers the least resistance to TMA adsorption.

The reactivity of a Au(111)-supported TiO_2(B)-(001)-I film to TMAA was also investigated [123]. High resolution (HR) XPS indicated that the acid is deprotonated to TMA, bonding to the surface in a bidentate manner similar to many carboxylates on rutile TiO_2(110) [175–178]. Unlike on rutile TiO_2(110), only half of the exposed Ti ions are coordinated due to the steric hindrance that would otherwise arise from their rather narrow spacing of 3.1 Å.

The reactivity of the TMA towards UV and synchrotron radiation was also investigated. It was found that TMA was photo-depleted with a reaction rate about twice that found on a reduced rutile TiO_2(110) surface. The difference was attributed to the lower concentration of reduced Ti species which participate in hole-annihilation.

2.3.3. Water. One of the major reasons why TiO_2 has been so well studied was the discovery by Fujishima and Honda that it photocatalyses the splitting of water [52, 53, 179], and it is this photoactivity which underpins the use of TiO_2 in numerous technologies such as self-cleaning surfaces [68], air/water purification devices [69], and solar cells [70]. Moreover, water is present in the vast majority of technological applications of TiO_2. As such, the interaction of water with TiO_2 surfaces is a crucial area of research [180] and naturally, the reactivity of water with several TiO_x thin films has been explored [94, 95].

The studied films were the *lepi*, TiO_2(B)-(001)-I, and star phases supported on Pt(111) [94] and the pinwheel, *hc*, TiO_2(B)-(001)-I, and star phases on Au(111) [95]. HR-XPS was used to investigate water adsorption on these films, and in the case of the Pt(111)-supported films, additional insights were also given from TPD and valence band (VB) photoemission measurements. The key indicator of the reactivity is the extent of water dissociation. In TPD, peak positions and shapes can be compared with those from the extensive literature on TiO_2 surfaces [180] and in HR-XPS the O1*s* peak can be monitored at the binding energies (BE) that are diagnostic for molecular water (~534 eV) and OH (~532 eV) [181, 182].

The *lepi* and star films could both be prepared as pure phases, i.e. without the co-existence of other TiO_x phases as could the TiO_2(B) phase on Au(111). However, the TiO_2(B) phase on Pt(111) co-existed with *z*-TiO_2, and the *hc*-TiO_2 and pinwheel phases on Au(111) co-existed with TiO_2 clusters.

It was concluded that the *lepi* and *hc* phases were unreactive towards water dissociation. For the *lepi* phase, no evidence

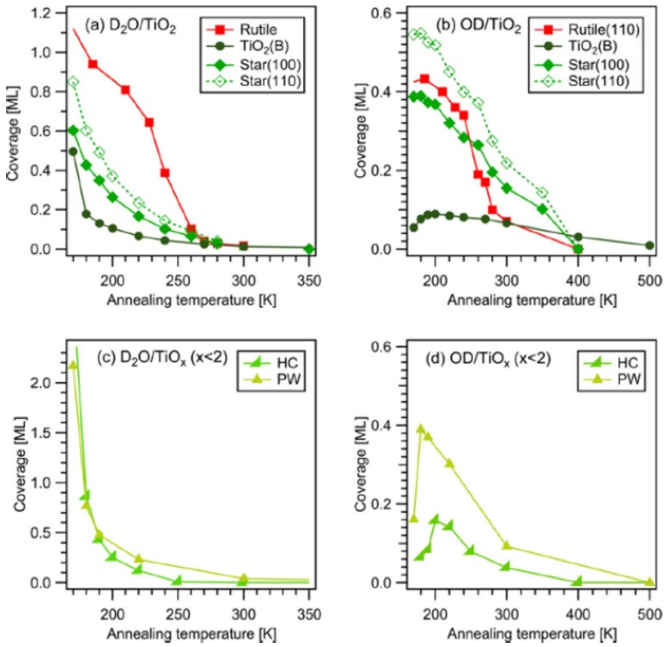

Figure 28. Coverages of (a) molecular water and (b) hydroxyl (OD) determined from HR-XPS for the TiO_2(B) and star phases supported on Au(111). The corresponding rutile TiO_2(110) coverages are plotted for comparison. 1 ML corresponds to the density of exposed surface Ti. For the star phase, the exact surface structure is unknown even though the structure is thought to be based on rutile (100). As such, the data is plotted twice [star(100) and star(110)] with 1 ML corresponding to the unreconstructed rutile (100) and the (110) faces, the latter to account for the possible microfacetting seen in the native phase. (c), (d) Equivalent plots for the *hc* and pinwheel (pw) phases. Reprinted with permission from [95]. Copyright (2015) American Chemical Society. (https://pubs.acs.org/doi/10.1021/acs.jpcc.5b00561) Further permissions related to the material excerpted should be directed to the ACS.

was found at all for water dissociation in line with calculations [183] whereas (deuterated) hydroxyl was observed in the HR-XPS for the *hc* phase as shown in figure 28(d). However, because the *hc* phase only accounts for ~79% of the areal coverage of TiO_x, the OD coverage was attributed to a minority of co-existing TiO_2 clusters.

TiO_2(B) was found to be slightly active for water dissociation, with a maximum coverage of 0.1 ML OD being detected on Au(111) at 200 K, as shown in figure 28(b). Likewise Pt(111)-TiO_2(B) was found to weakly dissociate water with OH being detectable in HR-XPS but not in the VB measurement. From TPD, a 10% contribution to the water desorption could be attributed to recombinative desorption, i.e. to OH. On the Au(111)-supported film, this dissociation was attributed to defects partly because the OH is comparatively stable to annealing with 40% of the maximum remaining up to 400 K and total removal only occurring at 500 K, reminiscent of the O_b-vacs on rutile TiO_2(110) [47, 180]. O-vacs are usually associated with Ti^{3+} and these are indeed detected, albeit with a greater proportion in the subsurface as judged by the greater relative intensity of that peak at normal compared with grazing emission angle [95]. On the other hand, on the

Pt(111)-supported film, it was concluded that the small amount of OH detected was not due to dissociation at Ti^{3+} because the OH has desorbed by 400 K. It is not yet clear what the difference is between these two TiO_2(B) films but a likely explanation is their different morphologies. On Au(111), TiO_2(B) wets the substrate more: about 90% of the surface is covered after 3 ML, whereas taller islands of TiO_2(B) grow on Pt(111) so that even after 4 ML, only about 50% of the surface is covered. So, for instance, active sites on the Au(111) film may be domain boundaries whereas active sites on the Pt(111) film may be at island edges. In addition, the co-existence with the z-TiO_2 film on Pt(111) may also have some influence on the observations [94].

The pinwheel phase is more active still, with a maximum OD coverage of 0.4 ML [see figure 28(d)]. This corresponds to about 20% of the Ti sites being able to dissociate water. This percentage tallies well with the density of Ti in the hubs and the spokes of the pinwheel and it was tentatively concluded that those were the active sites for water dissociation. At the same time the peak intensity of Ti 2p assigned to the pinwheel (and consistent with Ti^{2+}) decreases by 16% suggesting that those Ti species involved in water dissociation are oxidised in the reaction.

Like the pinwheel phase, the star phase on Au(111) is quite reactive, with a maximum OD coverage of about 0.4–0.5 ML, as shown in figure 28(b) [95]. This relatively high reactivity of the star phase was also found on Pt(111) with the recombinative desorption of hydroxyl making a 30% contribution to the water curve [94]. Artiglia *et al* [94] and Farstad *et al* [95] both make note of similarities with the results from native crystals of TiO_2(100) [184, 185] and in the latter case [95], behaviour somewhere between TiO_2(100) and TiO_2(110) which lends further support to the assignment of the star phase to TiO_2(100) and perhaps a reconstructed TiO_2(100) termination that contains TiO_2(110) microfacets.

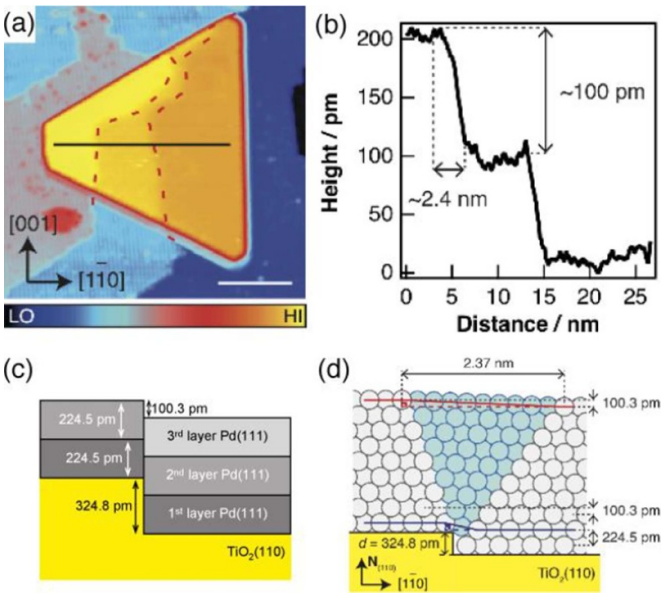

Figure 29. Pd step-island with a curved (111) top facet formed by carpet growth across the rutile TiO_2(110) step edge. (a) (450 Å)^2 STM image taken from a Pd nanoparticle spanning two step edges of the underlying TiO_2 substrate. The nanoparticle has a measured diameter of about 300 Å and a height of 19 Å. Red dashed lines roughly mark the locations of the step edges lying beneath the nanoparticle. The colour bar has a range of 22.3 Å and the scale bar (white) is 110 Å. (b) Line profile taken from the black line in (a). (c) Schematic model showing how the vertical misfit between TiO_2(110) and Pd(111) leads to ~100 pm steps. (d) Schematic showing a cross-section of a Pd nanocrystal spanning two adjacent rutile TiO_2(110) terraces. Pd(111) stacks with an interlayer spacing of 224.5 pm are placed on top of both TiO_2(110) terraces leading to a vertical mismatch of 100.3 pm between Pd(111) layers that originate from different terraces. This vertical mismatch is accommodated by formation of a 'carpet' region highlighted in blue. Reproduced with permission from [38].

3. Strain imparted on supported nanoparticles

We saw in section 2.1.1 for the rutile TiO_2(110) film grown on W(100) that the vertical mismatch could cause strain-induced crystallographic shear planes. If the situation is reversed and nanoparticles are grown on TiO_2(110), the vertical mismatch can also impart strain onto these nanoparticles.

When Pd is grown on TiO_2(110) and annealed below temperatures that induce encapsulation, large hexagonal islands grow that are terminated by Pd(111), evident from LEED and atomically-resolved STM [38].

While some Pd(111) islands reside at the TiO_2 terraces, others grow at step edges as shown in figure 29. So-called step-islands have curved tops as shown by the three colour levels in figure 29(a). The topography of the top facet essentially follows that of the underlying TiO_2(110) substrate. At the location of the TiO_2 steps, the height of the Pd(111) island changes. The line profile in figure 29(b) shows that the vertical separation between these levels is ~ 100 pm, much lower than the step height of Pd(111) (224.5 pm). As such, it was concluded that the Pd curves over the TiO_2 steps like a carpet. Figure 29(c) shows how a height of ~100 pm arises and figure 29(d) shows a ball model depicting the carpet growth.

When Pd(111) surfaces are covered by 0.33 ML CO at low temperature (~125 K or below), they only occupy hollow sites in a (H)-($\sqrt{3} \times \sqrt{3}$)$R30°$ configuration [186]. As the coverage increases towards 0.5 ML, bridge sites are also occupied so that bridge-bridge (BB) and hollow-hollow (HH) overlayers form with two CO molecules in a c(4 × 2) unit cell. Figure 30(a) shows an STM image from a step-island with a coverage of 0.5 ML CO. The same image is magnified and flattened in figure 30(b). The CO in the bottom of figure 30(b) is in a BB configuration. Two of the unit cells are drawn in light blue and there is an additional bright spot in the centre of the unit cell as would be expected from the BB configuration. At the top of figure 30(b), two unit cells are drawn in black. The unit cell is the same as that for BB except that the central spot is darker. The overlaid grid in figure 30(c) shows that the black unit cells correspond to atop-bridge (TB) occupation.

DFT calculations show that HH is the most stable configuration, followed by the BB configuration [38] as one would expect from the experimental observations of Rose *et al* [186]. To account for the occupation of atop sites observed

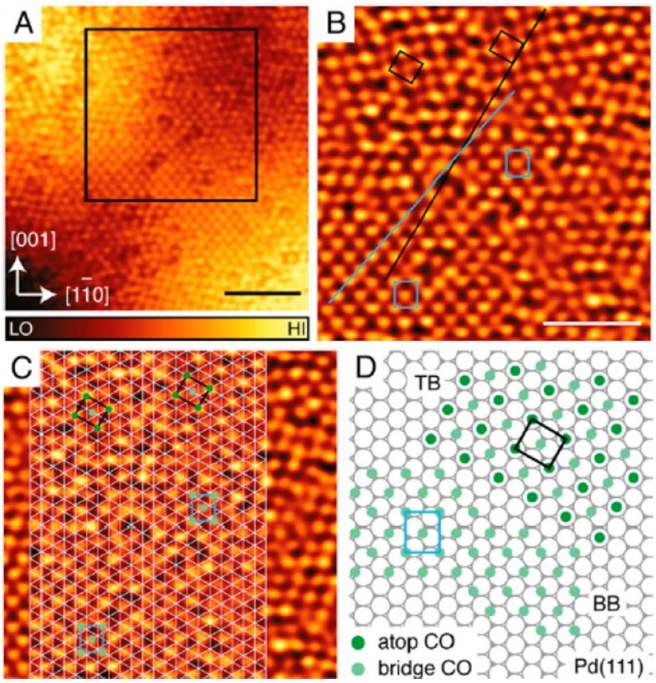

Figure 30. C(4 × 2)-2CO structures with TB and BB site occupations on a curved Pd(111) nanocrystal. (a) (120 Å)^2 STM image (78 K) recorded from a Pd step-island covered with 0.5 ML CO. The colour bar has a range of 77 pm and the scale bar is 30 Å. (b) (69 Å)^2 image magnified from the square marked in (a) and flattened by applying a band-pass filter. Two separate BB regions are highlighted with light blue unit cells and two separate TB regions are marked with black unit cells. The scale bar is 20 Å. (c) As B, with a perfect hexagonal grid superimposed on part of the image. The positions of Pd atoms are marked by interstices in the grid. The registration of the STM spots with the grid confirms the presence of both BB and TB overlayers. Some CO in atop and bridge positions are marked dark- and light-green, respectively. (d) Ball model showing TB (top right) and BB (bottom left) configurations. Reproduced with permission from [38]

in STM, Yim *et al* [38] suggest that the strained lattice in the step-islands may be responsible for the stabilization of the TB configuration. In figure 29, the Pd in the blue wedge is strained so that the Pd lattice is elongated along the step direction.

Yim *et al* [38] set up a model system in order to assess the effect of strain on the adsorption of CO on Pd. Tensile strain was modelled by elongation along Pd[$\bar{1}$01] together with compression in the orthogonal direction and vice versa for compressive strain. The ratio between the applied tensile and orthogonal compressive strains was set at 0.39, equal to the Poisson ratio for bulk Pd. While the hierarchy of stability does not change with the strained samples, the calculations show that the energy gap between different phases decreases under both tensile and compressive strain, so that the TB configuration becomes competitive with HH. Thus it was concluded that the carpet growth introduced strain into the Pd nanoparticle which made the TB configuration stable enough to be observed in the STM images.

Apart from the strain that arises from the vertical misfit of Pd(111) on rutile TiO_2(110), there is also an influence from the lateral misfit. Harding *et al* [39] used XRD to measure the out-of-plane lattice parameter of a 164 Å thick Pd(111) film also grown on rutile TiO_2(110). From that, the in-plane strain and stress were computed. For simplicity, the anisotropy of the TiO_2 surface was ignored, giving in-plane strain and stress in the Pd film of 0.29% and 0.83 GPa, respectively. To test the reactivity of these Pd(111) films against native Pd(111), molecular beams of CO were directed at the sample and the subsequent rate of desorption was measured using velocity-resolved kinetics (VRK) [187, 188]. These measurements were made at high temperature (~800 K) so the strain and stress values were recalculated at 803 K. Taking into account the anisotropic thermal expansion coefficient of the rutile substrate, this gives a strain of 0.06% in the TiO_2[001] direction and 0.17% in the [1$\bar{0}$] direction. The stress differs less in the two directions being 0.28 and 0.38 GPa in those same directions, respectively.

Analysis of the VRK data shows that the binding energy of CO is greater on the Pd(111) film at 164 kJ mol^{-1} compared with the 124 kJ mol^{-1} found using the same method on single crystal Pd(111) [39, 187] and this change was attributed to the strain in the Pd(111) film. The calculations of Yim *et al* [38] are in qualitative agreement, showing that the adsorption energy is increased for small values of either compressive or tensile strain. However, these studies cannot be compared directly because the nanoparticles in the work of Harding *et al* [39] are an order of magnitude taller than those of Yim *et al*. The temperature of the VRK measurements were also beyond that where a transition to just hollow site occupation has been found [189].

Au nanoparticles have also been studied at steps on rutile TiO_2(110) using scanning transmission electron microscopy (STEM) [190]. The TiO_2 samples were prepared by ion milling at 5 kV, after which a hole was created in the centre. The crystal was then annealed in air at 1273 K to form edge facets. The resulting facets are 'miscut' from the perfect (110) plane and can be described as (110) but with regularly-spaced steps. Au was deposited onto the sample in vacuum but the nanoparticles were grown by annealing in air. These nanoparticles have a variety of shapes but those with (111) top facets dominate and were the only ones analysed. Additionally only low miscut surfaces were considered, i.e. those with rotations less than 18° from the perfect (110) plane.

These Au nanoparticles have widths of ~30–60 Å and heights of 15–40 Å, so the heights are comparable to those in the work of Yim *et al* [38] but the widths are about an order of magnitude narrower.

The STEM images show that the rotation angles of the Au nanoparticles are much lower than those of the TiO_2 substrates and the spread is much narrower too, ranging from 0–6° on surfaces with miscut angles of ~7–18°.

Figure 31(a) shows an image of one of these nanoparticles. The rotation angle of the nanoparticle is 5.7° on a 9.7° miscut TiO_2 surface. The image also shows that 4 atomic columns of TiO_2 coincide with 5 Au columns [102]. At the interface, the Au is particularly deformed, even containing several vacancies. In the layers above, even though the lattice displacement

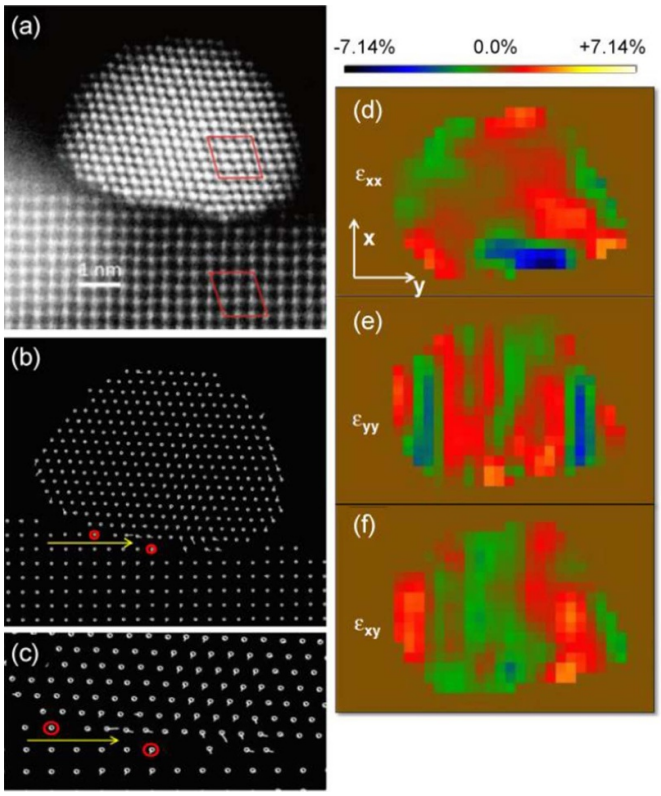

Figure 31. (a) High angular annular dark field (HAADF) STEM image of Au nanoparticle on a 9.7° miscut rutile TiO_2 surface. The red box indicates the coincident site lattices [102] of the Au nanoparticle and the TiO_2 surface. (b) Atomic displacements measured from (a). Undistorted positions are marked with circles and displacements are shown with arrows. (c) A magnified section of (b). The red circles are used as registration marks. (d)–(f) Strain maps for the Au nanoparticle based on the displacements for normal strain in x (ε_{xx}) and y (ε_{xx}) directions and shear strain (ε_{xx}). Reprinted from [190], Copyright (2014), with permission from Elsevier.

is much reduced, the carpet-like growth is observable, similar to that in the work of Yim *et al* [38].

A quantitative assessment of the strain was made using a lattice analysis method known as template-matching analysis (TeMa) which measures the local deviation from a template created from averaging over a group of atomic columns [191] in the STEM. The atomic displacements are shown alongside the image in figures 31(b) and (c). Large displacements of 0.65 Å are seen at the interface. These displacements are largely horizontal at the terraces and vertical at the step. As can also be seen in the raw image, displacements are much lower away from the interface. Strain maps for ε_{xx}, ε_{yy}, and ε_{xy} were calculated from these displacements and shown in figures 31(d)–(f). In the x direction, the nanoparticle is compressed near the step and a small tensile strain is seen near the top and the bottom corners. In the y direction, there is an expansion near the Au/TiO_2 interface. For the shear strain, ε_{xy}, the strain reaches −4.9% at the step but is only 0.7% at the surface of the nanoparticle.

A modified Wulff-Kaishew analysis of the equilibrium nanoparticle shapes show that the interface energy is lower at

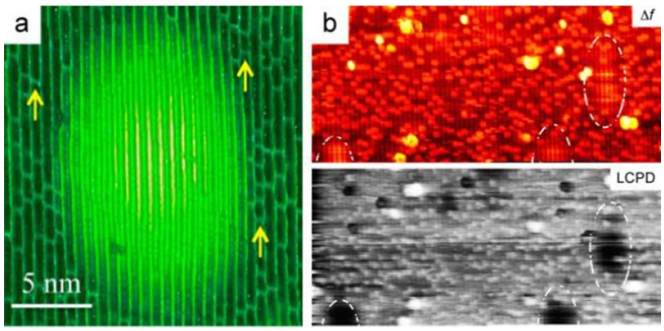

Figure 32. (a) STM image of a protrusion after Ar-sputtering at high temperatures. Reprinted with permission from [41]. Copyright (2015) American Chemical Society. (b) 475 Å × 210 Å NC-AFM frequency shift (top) and local contact potential difference (bottom) images of TiO_2(110) recorded with Kelvin probe control. Reproduced from [204]. CC BY 4.0.

0.48 J m^{-2} compared with 0.61 J m^{-2} [192] found for Au nanoparticles on a flat TiO_2(110) surface which implies a stronger Au-TiO_2 interaction than on the flat surface.

4. Embedded nanoparticles

The subsurface of materials can also influence the surface properties. While this is probably most evident in the doping of semiconductors [193], there is also an extensive body of work focused on doping of TiO_2, largely with the purpose of improving its photocatalytic efficiency [194] but also as a means of imparting magnetism [195, 196].

When Cr was deposited on a $SrTiO_3$(001)-supported anatase TiO_2(001) film and annealed, the ridges that form the (1 × 4) reconstruction (see figure 6) became branched, giving a wavy appearance [197]. It was suggested that the doped Cr in substitutional and/or interstitial sites disrupts the delicate stress-stability balance of the ADM structure [109, 111] giving rise to this disordered reconstruction.

In a series of experiments, Osgood and co-workers implanted Ar nanoparticles in the rutile TiO_2(110) surface by sputtering with Ar ions at elevated temperature [40–42]. This led to the appearance in STM of elliptical bumps elongated in the [001] direction, as shown in figure 32(a).

Similar looking bumps have been observed in STM images of TiO_2(110) prepared in the typical fashion (sputtering at room temperature followed by annealing at ~800–1000 K). These bumps were attributed to individual positively-charged defects buried beneath the surface, possibly substitutional V^{5+} [198–200]. The bumps arise from local band bending and have also been observed in STM images of several conventional semiconductors [201, 202] as well as ZnO(000$\bar{1}$)-O [203]. The charged nature of these buried defects in TiO_2(110) was confirmed in maps of the local contact potential difference obtained simultaneously with non-contact atomic force microscopy (NC-AFM), as shown in figure 32(b) [204].

The heights of these bumps on the typically-prepared rutile TiO_2(110) seem to be limited to a few Å whereas those

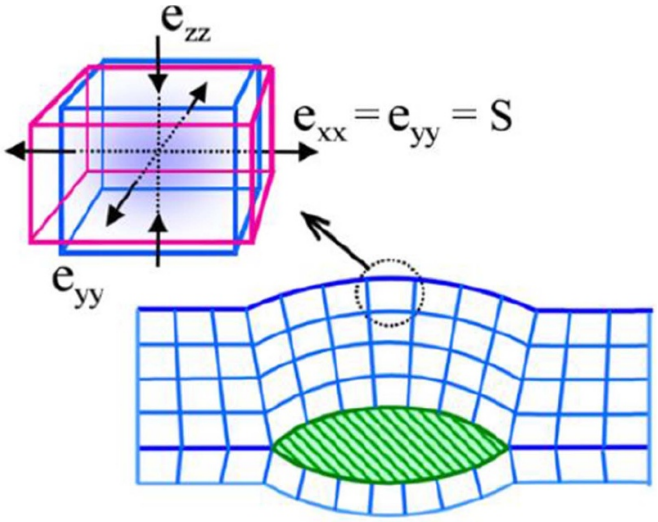

Figure 33. Drawing to illustrate the origin of elastic surface strain field, showing different components of elastic strain from a portion of the solid at the centre of a bump. Reprinted with permission from [42]. Copyright (2016) American Chemical Society.

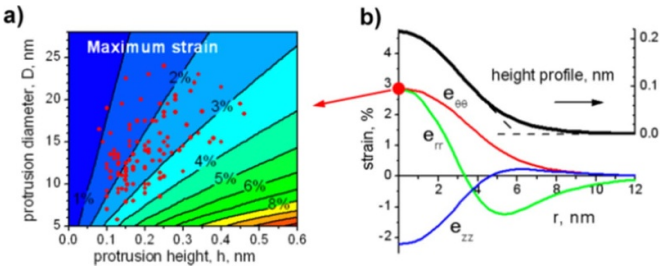

Figure 34. Surface strain values derived from the continuum mechanics model. (a) Colour map of the maximum strain (at $r = 0$) as a function of the dimensions of the bumps. The red points represent the dimensions of the bumps collected from STM images. (b) Strain components on the surface of a circular bump as a function of the radial distance, r, calculated from the continuum model. The profile of this protrusion is shown with the black curve. The red, green, and blue curves represent tangent ($e_{\theta\theta}$), radial (e_{rr}), and vertical (e_{zz}) components of strain, respectively. The maximum tensile strain is marked with the red circle; this value is represented in the colour map in (a). Reprinted with permission from [40]. Copyright (2014) American Chemical Society.

observed by Osgood *et al* reach a height of 10 Å, with widths up to 300 Å. Osgood *et al* therefore attribute their bumps to a different origin, i.e. the accumulation of interstitial Ar into clusters beneath the surface by analogy with observations on metal substrates [5, 205]. Similar bumps or so-called blisters were also observed following He ion bombardment of rutile TiO_2(100) supported on α-Al_2O_3(0001) [91].

Such bumps lead to a strained surface as illustrated in figure 33. Potapenko *et al* quantified the strain at the bumps by applying a continuum mechanics model [40], a method demonstrated previously on single crystals of $LiNbO_3$ [206]. The calculated surface strain is mapped against the widths and heights of the bumps in figure 34(a). The red points correspond to the bumps measured in STM and indicate maximum strain values of ~2–4%. Figure 34(b) shows components of the strain as a function of the radial distance, r, all of which reach their maximum values at the centre.

Although the atomic structure above the buried Ar clusters is basically the same as on the flat surface, the area is devoid of O_b-vacs, presumably due to the strain at these bumps [40, 41]. DFT calculations (which will be discussed in more detail in section 5) show that applying tensile or compressive strain can move the most favourable oxygen vacancy site from the bridging O to subsurface/in-plane oxygen [43–45] as well as affecting properties such as the diffusion of oxygen vacancies and the dissociation of water [45, 207]. Given the strain values used in the DFT calculations in refs [43–45] was about 2–3%, comparable with that found by Potapenko *et al,* this certainly looks like an area rich for further investigation.

Li *et al* [41] and Potapenko *et al* [42] observed that bridging hydroxyl (OH_b) were found on these bumps but that their concentration was noticeably lower than that on the flat regions. Given that these OH_b result from the dissociation of water at O_b-vacs [208–210] their presence at the bumps must arise from diffusion [209, 211]. Because of their relatively high mobility, Potapenko *et al* [42] conclude that the surface concentration of OH_b at the bumps have a Boltzmann distribution and can be expressed as follows:

$$\frac{C_{bump}}{C_{flat}} = exp\left(\frac{\Delta E}{kT}\right) \quad (1)$$

where C_{bump} is the average concentration of OH_b in a bump and C_{flat} is the average concentration of OH_b in the surrounding flat areas of the same terrace that contained the bump. Both C_{bump}/C_{flat} and ΔE were plotted against the maximum horizontal surface strain, S, of each bump as shown in figure 35.

A small number of bumps contain no OH_b at all [circled in figure 35(a)]. This gives rise to an unphysical infinite solution to equation (1). It is not clear why these minority bumps do not contain OH_b at all, although it is worth noting that the bumps caused by buried positively-charged defects are also devoid or nearly devoid of OH_b because they are also positively charged and therefore repelled by the defects [204].

If the small number of bumps that contained no OH_b are ignored, it can be seen that C_{bump}/C_{flat} and ΔE are approximately proportional to S. This means that bumps with higher strain contain fewer OH_b.

Thus, this work shows that the local strain can directly affect the distribution of O_b-vacs and OH_b, both of which are important elements of the rutile TiO_2(110) reactivity [46–48, 208–214].

5. Strain-induced property changes

While we have seen numerous examples of strained nanostructures in this review, except for in a few cases, the effects of stress and strain on the material properties have not yet been

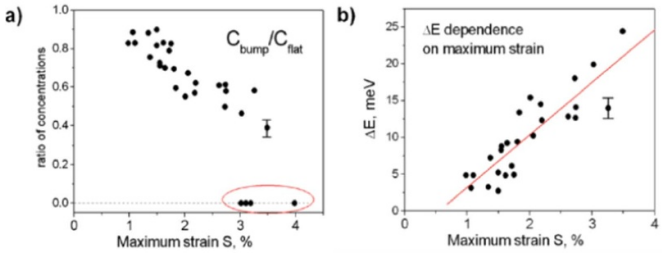

Figure 35. (a) Distribution of OH_b concentration on protrusions (normalized to that on the flat surface) as a function of the maximum strain value, *S*. (b) Distribution of the calculated total OH_b energy shift on the protrusions, ΔE, as a function of surface strain, *S*. Reprinted with permission from [42]. Copyright (2016) American Chemical Society.

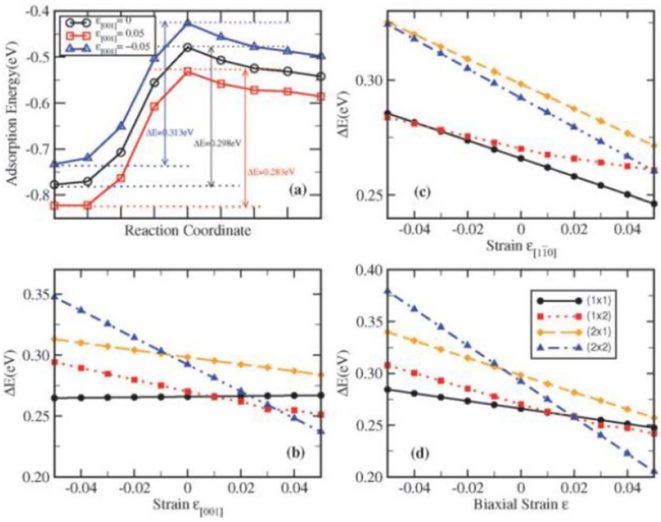

Figure 36. (a) Variation of the energetics during water dissociation on a $TiO_2(110)$ surface with a (2×1) water overlayer under different strains along the [001] direction. The water dissociation barrier (ΔE) as a function of the strain applied (b) uniaxially along the [001] direction, (c) uniaxially along the $[1\bar{1}0]$ direction, and (d) biaxially. Reproduced from [207] with permission of The Royal Society of Chemistry, permission conveyed through Copyright Clearance Center Inc.

elucidated. However, studies on free-standing titania nanostructures [56–61] and theoretical calculations indicate that strain can have a decisive effect [43–45, 49–51, 207].

Shu *et al* [43] and Wang *et al* [45] used DFT calculations to show that the formation energies of different types of O-vacs on rutile $TiO_2(110)$ change depending on the applied strain. The vacancies considered are O_b-vacs, sub-O_b-vacs, and in-plane O vacs. The oxygen atoms from which the vacancies are formed are labelled in figure 1. As one would expect [46–48, 208, 209, 215], on the unstrained surface, O_b-vacs are the most stable. Under compressive strains greater than 2%, applied in either the $[1\bar{1}0]$ or [001] direction, the sub-O_b-vac becomes the most stable vacancy. The in-plane vacancy becomes the most stable with tensile strain of 2.5% in the $[1\bar{1}0]$ direction.

When biaxial strain is applied [45], similar general trends are observed: sub-O_b-vac is favoured with compression in either direction whereas in-plane O-vac is favoured mainly by expansion in $[1\bar{1}0]$.

We saw in section 2.1.1 that on Ag(100), the $TiO_2(110)$ surface is uniaxially compressed in the [001] direction by 2.4% [14]. According to the calculations, the dominant vacancies should be sub-O_b-vacs. Normally, $TiO_2(110)$ surfaces are decorated with surface O_b-vacs or OH_b that result from dissociation in those O_b-vacs [208–211]. These point defects were not observed in STM images of the Ag(100)-$TiO_2(110)$ sample [14]. However, because point defects are sometimes invisible to STM depending on the condition of the tip [216], more work would be required before that observation could be linked to the strain in the rutile film.

As briefly discussed in section 4, the Ar-induced bumps reported by Osgood and co-workers [40–42] lead to $TiO_2(110)$ regions under tensile strain, albeit not homogenously applied. These strains reach up to 4% where in-plane O-vacs are favoured according to the calculations [43–45]. Interestingly, O_b-vacs are absent from the STM images of these bumps and a shift to in-plane vacancies is a possible explanation, although again more work would be needed to test this idea.

Wang *et al* [45] also show that when tensile strain is applied along $[1\bar{1}0]$ direction, the barrier to a concerted O_b-vac diffusion route is lowered. It should be noted, however, that their calculations favour this diffusion route even without any applied strain whereas experiments have so far only detected diffusion in the [001] direction [215].

The effect of strain on water adsorption on the undefected, perfect $TiO_2(110)$ surface was also investigated by Yang *et al* [207]. As shown in figure 36, they found that tensile strain in either the $[1\bar{1}0]$ or [001] directions leads in general to a decrease in the barrier to water dissociation. This effect was strongest when the water coverage was the lowest, i.e. with a (2×2) water layer, and weakest at the highest coverage, i.e. with a (1×1) water layer. In fact for the case of uniaxial strain in the [001] direction, there is a slow rise in the dissociation barrier for the (1×1) layer.

Like $SrTiO_3$ [8, 12, 217], rutile TiO_2 is classed as an incipient ferroelectric material: its dielectric permittivity increases dramatically as the temperature decreases but no ferroelectric transition occurs even at 0 K [218–220]. A room temperature ferroelectric phase transition was induced on $SrTiO_3$ by applying biaxial in-plane strain via the growth of thin films of $SrTiO_3(001)$ on slightly lattice-mismatched substrates [8].

DFT calculations indicate that a ferroelectric transition may also be induced in rutile TiO_2 and for supported (110) thin films [221, 222]. In rutile TiO_2, the incipient ferroelectric behaviour has been traced to a soft, long wavelength transverse optical (TO) A_{2u} mode, the so-called ferroelectric mode [219, 220]. By monitoring the frequency of the TO A_{2u} mode, Montanari and Harrison show that application of an isotropic negative pressure of ~−4 GPa would induce a ferroelectric phase transition [221]. Likewise, their calculations show that a ferroelectric phase transition would also occur if a uniaxial tensile strain of 3% was applied in the [001] direction as shown in figure 37.

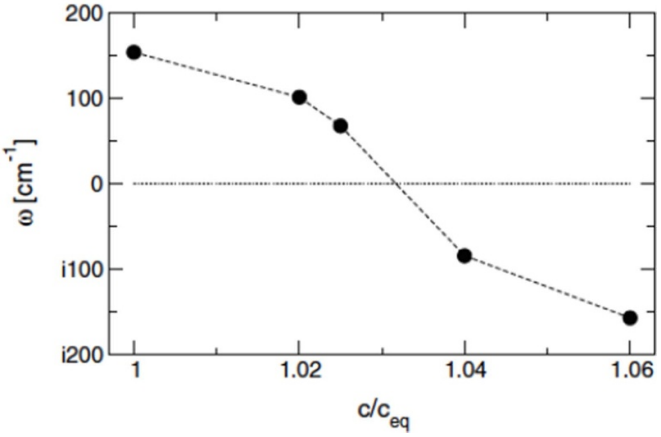

Figure 37. Harmonic frequency of the TO A_{2u} vibrational mode as a function of uniaxial strain along the c axis (here the c axis is the [001] direction). c is the length of the lattice and c_{eq} is the unstrained lattice constant. Note that the frequency goes to zero near $c/c_{eq} = 1.03$. Reproduced from [221]. © IOP Publishing Ltd. All rights reserved.

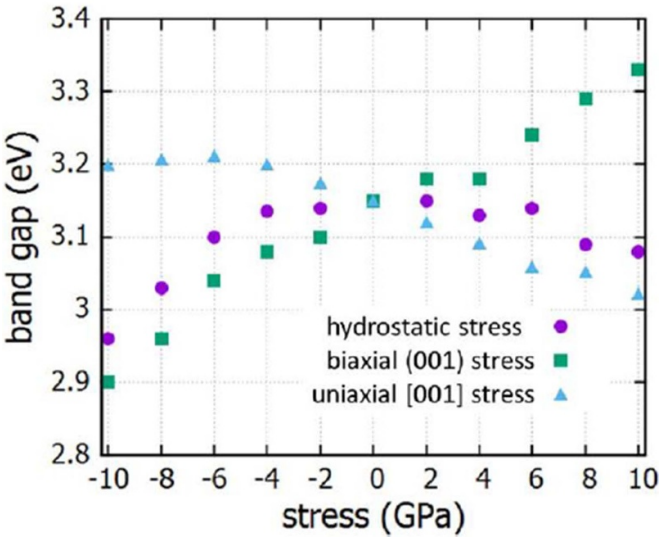

Figure 38. Variations of the calculated band gap for anatase with applied hydrostatic, biaxial and uniaxial stress. Positive stress corresponds to compressive stress. The uniaxial stress is applied along the [001] direction (or c). Biaxial stress is applied along the [100] and [010] directions (a and b). Reproduced from [51]. CC BY 4.0.

Later calculations by Grünebohm *et al* [222–224] and Ni *et al* [225] also found a softening of this TO A_{2u} mode when tensile strain was applied in the [001] direction. In addition to this, Grünebohm *et al* also found a softening of this mode when tensile strain was applied in the [110] direction whereas Mitev *et al* [226] found this mode to be almost independent of [110] strain. These conflicting results were attributed to differences in the computational methodologies employed [227, 228].

By extending their models to explicitly treat a thin rutile TiO_2(110) film, the calculations of Grünebohm *et al* [222] indicate that the ferroelectric behaviour can also be stabilised at the surface with tensile uniaxial strains in the region of 2% in either [001] or [$\bar{1}$10]. While rutile TiO_2(110) has been shown to be uniaxially compressed by 2.4% in the [001] direction on Ag(100), compressive strain has not been shown to stabilise a ferroelectric phase on rutile. Although no rutile (110) phases reported in section 2.1.1 have tensile strain, if an appropriately lattice mismatched substrate was found [229] then the possible existence of ferroelectric phases could be investigated. On the other hand, if the star phase on Pt(111) really has the rutile (100) structure, then it would be a candidate for such studies as its lattice would be expanded by ~6% in both [001] and [010].

The effect of stress and strain has also been explored on anatase using DFT. Recent DFT + U calculations show that biaxial tensile stress applied in the a and b directions leads to a decrease in the band gap to 2.9 eV at 10 GPa, as shown in figure 38 [51]. Likewise, uniaxial compressive stress applied in the c direction leads to a decrease in the band gap to just above 3 eV. The same trends were obtained in earlier calculations [49, 50]. In contrast to these findings for anatase, calculations on rutile do not yield nearly as much change in the band gap. This is because while anatase has one soft axis of compressibility, rutile has two orthogonal soft axes, [1$\bar{1}$0] and [110], and therefore no overall soft direction [50].

Simpson *et al* [55] detected a 100 meV redshift in the band gap going from anatase grown on $LaAlO_3$ ($a = 3.78$) to that grown on $SrLaGaO_4$ ($a = 3.84$ Å). Although, the film morphology is not described it is likely to be of anatase (001) character given that the size of lattice misfit (+1.4%) puts it comfortably within the range where Apgar and Martin find that the (001) termination is favoured [100]. This redshift is consistent with the calculations for bulk anatase which predict a decrease in the band gap with expansion of the in-plane anatase lattice parameter.

A recent study by Rajender and Giri [56] concerning free-standing TiO_2 nanoparticles also showed a decreased band gap due at least partly to strain. In their work, TiO_2 powder with anatase character was ball-milled in ambient conditions in order to introduce strain. Although the milling process will apply stress along multiple directions, the soft direction should be affected most which according to the calculations above should lead to a band gap reduction. By analysis of XRD and HRTEM images, Rajender and Giri found that the strain was maximised after milling for 16 h beyond which the strain was relieved. The band gap was found to be 3.14 eV without milling and 2.71 eV after 16 h milling. After 40 h, the band gap increased again to 2.79 eV, following the same trend as the strain. It was therefore concluded that the strain was the main cause of the band gap reduction although some contribution was also attributed to lattice defects such as O-vacs.

As we saw in section 2.1.2, calculations show that the reactivity of the anatase (001)-(1 × 4) surface changes depending on the strain: a 3% compression made the surface inert and a ~2% expansion made it more reactive [111]. In fact, the stability of the ADM model and various closely-related models

(several of which differ only in having additional vacancies, interstitial Ti, and O adatoms) were shown to change as a function of the strain [111]. As was mentioned in section 2.1.2, there are differing reports on the reactivity of the anatase (001)-(1 × 4) surface [28, 29, 108, 112]. Tang *et al* [29] suggest one possible reason for the discrepancies may be that results are taken from both thin film and mineral samples and that the mineral samples may have their properties altered by impurity dopants. The level of strain across these different samples provides another possible explanation.

6. Outlook

In this review, we have seen numerous examples of how stress and strain is manifested in TiO_x nanostructures. The majority of examples are related to thin films. Epitaxial misfit leads to strain in the thin film. By changing the substrate, the same TiO_x films can be prepared with different degrees of strain. In principle, this allows the properties of differently-strained TiO_x films to be probed systematically. One important property predicted to change with the degree of strain is the band gap of anatase TiO_2. This has already been supported by one experimental observation discussed in section 5 for anatase (001) on $LaAlO_3$ *vs*. $SrLaGaO_4$ [55]. While anatase has mainly been grown on $SrTiO_3$(001) and $LaAlO_3$(001), these substrates themselves can have their lattice spacing tuned by substitution of different cations [12], which would allow for a much more finely graduated array of strained anatase films. One such complex oxide substrate, $(LaAlO_3)_{0.3}$-$(Sr_2AlTaO_6)_{0.7}$, was successfully employed by Apgar and Martin to grow anatase (001) as discussed in section 2.1.2 [100]. Another strategy is to grow one oxide support on top of another before adding the anatase film as Wang *et al* did with a $SrTiO_3$-$BaTiO_3$-anatase (001) film [230]. Employing $BaTiO_3$ may even allow for an additional perturbation of the strain via piezoelectric control, although any such deformations would be quite small [231].

In addition to optical methods for determining the band gap [55], scanning tunnelling spectroscopy (STS) can also be used. Indeed special regions or phases with reduced band gaps have already been identified on rutile TiO_2(011) [232] and anatase TiO_2(101) [233] in this way.

Comparisons between different films can be complicated by the co-existence of different phases. For instance, more rutile was found to be present in anatase films grown on $SrTiO_3$(001) compared with $LaAlO_3$(001) [22]. While the measurement field-of-view can be selected to eliminate this complication for scanning probe-based techniques such as STS, many other techniques rely on ensemble-averaging measurements. Careful characterization of the film quality is essential to such measurements. Some films are more suited to such investigations. For example, because the lepidocrocite-like films tend to spread across the entire surface and are self-limited to a bilayer, comparing across different substrates should be more straightforward, and table 4 shows that there is a already a good spread of strain values accessible from the substrates used to date.

As we saw, there has already been significant research effort aimed at using strain-relief structures to template the ordered growth of adsorbates such as metal nanoparticles and organic molecules and this is likely to continue apace.

While Au nanoparticles were the focus in this review, calculations have shown subtly different behaviour for Pd nanoparticles on the z and z' phases compared with Au nanoparticles [172]. We have also seen that Au nanoparticles are pinned at the hubs of the pinwheels on Rh(111) and Au-Pd(111) [34, 35] but it is not yet known to what extent this would apply to other metal nanoparticles and pinwheels supported on other substrates.

Similarly, while TMAA has been shown to preferentially dissociate near the hubs of the pinwheels, the details of the reaction mechanism have not yet been fully elucidated. Understanding these issues will contribute to our ability to employ such films for the ordered self-assembly of nanoparticles and organic molecules, a step towards building functional materials with a bottom-up approach.

The strain transferred to supported nanoparticles and caused by buried nanoparticles are areas with much potential. Although the details are different, the studies by Yim *et al* [38] and Harding *et al* [39] clearly show a different reactivity for supported Pd(111) nanoparticles compared to single crystal Pd(111) and this is likely to also apply to other supported nanoparticles. Likewise, the reactivity of rutile TiO_2(110) was modified by the presence of subsurface Ar nanoparticles [40–42]. One could envisage a surface with ordered, strained regions designed by growing TiO_x films over substrates that themselves have ordered protrusions or depressions.

ORCID iD

Chi Lun Pang https://orcid.org/0000-0002-5222-9734

References

[1] Sato H and Naito M 1997 *Physica* C **274** 221
[2] Locquet J-P, Perret J, Fompeyrine J, Mächler E, Seo J W and Van Tendeloo G 1998 *Nature* **394** 453
[3] Garcia-Barriocanal J, Rivera-Calzada A, Varela M, Sefrioui Z, Iborra E, Leon C, Pennycook S J and Santamaria J 2008 *Science* **321** 680
[4] Brune H, Giovannini M, Bromann K and Kern K 1998 *Nature* **394** 451
[5] Gsell M, Jakob P and Menzel D 1998 *Science* **280** 717
[6] Süess M J, Geiger R, Minamisawa R A, Schiefler G, Frigerio J, Chrastina D, Isella G, Spolenak R, Faist J and Sigg H 2013 *Nat. Photon.* **7** 466–72
[7] Beach R S, Borchers J A, Matheny A, Erwin R W, Salamon M B, Everitt B, Pettit K, Rhyne J J and Flynn C P 1993 *Phys. Rev. Lett.* **70** 3502–5
[8] Haeni J H *et al* 2004 *Nature* **430** 758–61
[9] Men FK, Packard WE and Webb MB 1988 *Phys. Rev. Lett.* **61** 2469
[10] Uesugi-Saitow Y and Yata M 2002 *Phys. Rev. Lett.* **88** 4
[11] Fujita D, Kitahara M, Onishi K and Sagisaka K 2008 *Nanotechnology* **19** 025705
[12] Hwang J *et al* 2019 *Mater. Today* **31** 100–18
[13] Lai X, Guo Q, Min B K and Goodman D W 2001 *Surf. Sci.* **487** 1–8

[14] Atrei A, Cortigiani B and Ferrari A M 2012 *J. Phys. Condens. Matter* **24** 445005
[15] McCavish N D and Bennett R A 2003 *Surf. Sci.* **546** 47–56
[16] Bennett R A and McCavish N D 2005 *Top. Catal.* **36** 11
[17] Bennett R A, Mulley J S, Newton M A and Surman M 2007 *J. Chem. Phys.* **127** 084707
[18] Matharu J, Cabailh G and Thornton G 2013 *Surf. Sci.* **616** 198–205
[19] Pang C L, Grinter D C, Matharu J and Thornton G 2013 *J. Phys. Chem.* C **117** 25622–7
[20] Herman G S and Gao Y 2001 *Thin Solid Films* **397** 157–61
[21] Murakami M, Matsumoto Y, Nakajima K, Makino T, Segawa Y, Chikyow T, Ahmet P, Kawasaki M and Koinuma H 2001 *Appl. Phys. Lett.* **78** 2664–6
[22] Kennedy R J and Stampe P A 2003 *J. Cryst. Growth* **252** 333–42
[23] Sugimura W, Yamazaki A, Shigetani H, Tanaka J and Mitsuhashi T 1997 *Jpn. J. Appl. Phys.* **36** 7358
[24] Sasahara A, Droubay T C, Chambers S A, Uetsuka H and Onishi H 2005 *Nanotechnology* **16** 16–19
[25] Krupski K, Sanchez A M, Krupski A and McConville C F 2016 *Appl. Surf. Sci.* **388** 684–900
[26] Herman G S, Sievers M R and Gao Y 2000 *Phys. Rev. Lett.* **84** 3354
[27] Liang Y, Gan S, Chambers S A and Altman E I 2001 *Phys. Rev.* B **63** 1–7
[28] Wang Y *et al* 2013 *Nat. Commun.* **4** 22144
[29] Tang H, Cheng Z, Dong S, Cui X, Feng H, Ma X, Luo B, Zhao A, Zhao J and Wang B 2017 *J. Phys. Chem.* C **121** 1272–82
[30] Potapenko D V and Osgood R M 2009 *Nano Lett.* **9** 2378–83
[31] Ragazzon D, Schaefer A, Farstad M H, Walle L E, Palmgren P, Borg A, Uvdal P and Sandell A 2013 *Surf. Sci.* **617** 211–7
[32] Cavaliere E, Artiglia L, Rizzi G A, Gavioli L and Granozzi G 2013 *Surf. Sci.* **608** 173–9
[33] Li Z, Potapenko D V and Osgood R M 2014 *J. Phys. Chem.* C **118** 29999–30005
[34] Mutombo P, Gubó R and Berkó A 2016 *J. Phys. Chem.* C **120** 12917–23
[35] Gubó R, Yim C M, Allan M, Pang C L, Berkó A and Thornton G 2018 *Top. Catal.* **61** 308–17
[36] Campbell C T 1997 *Surf. Sci. Rep.* **27** 1
[37] Henry C R 1998 *Surf. Sci. Rep.* **31** 231–3
[38] Yim C M, Pang C L, Hermoso D R, Dover C M, Muryn C A, Maccherozzi F, Dhesi S S, Pérez R and Thornton G 2015 *Proc. Natl Acad. Sci. USA* **112** 7903–8
[39] Harding D J, Bongers M D, Wagner S, Hahn H, Neugebohren J, Kitsopoulos T N, Wodtke A M and Pundt A 2019 *J. Phys. Chem.* C **123** 12255–60
[40] Potapenko D V, Li Z, Kysar J W and Osgood R M 2014 *Nano Lett.* **14** 6185–9
[41] Li Z, Potapenko D V and Osgood R M 2015 *ACS Nano* **9** 82–87
[42] Potapenko D V, Gomes G T and Osgood R M 2016 *J. Phys. Chem.* C **120** 21373–80
[43] Shu D J, Ge S T, Wang M and Ming N B 2008 *Phys. Rev. Lett.* **101** 116102
[44] Shu D J, Ge S T, Wang M and Ming N B 2011 *Phys. Rev. Lett.* **106** 39902
[45] Wang Z W, Shu D J, Wang M and Ming N B 2010 *Phys. Rev.* B **82** 165309
[46] Diebold U 2003 *Surf. Sci. Rep.* **48** 53–229
[47] Pang C L, Lindsay R and Thornton G 2008 *Chem. Soc. Rev.* **37** 2328–53
[48] Pang C L, Lindsay R and Thornton G 2013 *Chem. Rev.* **113** 3887–948
[49] Thulin L and Guerra J 2008 *Phys. Rev.* B **77** 1–5
[50] Yin W J, Chen S, Yang J H, Gong X G, Yan Y and Wei S H 2010 *Appl. Phys. Lett.* **96** 221901
[51] Kelaidis N, Kordatos A, Christopoulos S-R G and Chroneos A 2018 *Sci. Rep.* **8** 1–8
[52] Hashimoto K, Irie H and Fujishima A 2005 *Jpn. J. Appl. Phys.* **44** 8269–85
[53] Fujishima A, Zhang X and Tryk D A 2008 *Surf. Sci. Rep.* **63** 515–82
[54] Henderson M A 2011 *Surf. Sci. Rep.* **66** 185–297
[55] Simpson J R, Drew H D, Shinde S R, Choudhary R J, Ogale S B and Venkatesan T 2004 *Phys. Rev.* B **69** 2–5
[56] Rajender G and Giri P K 2016 *J. Alloys Compd.* **676** 591–600
[57] Kim Y, Watanabe M, Matsuda J, Staykov A, Kusaba H, Takagaki A, Akbay T and Ishihara T 2020 *J. Mater. Chem.* A **8** 1335–46
[58] Wang X, Li Z, Shi J and Yu Y 2014 *Chem. Rev.* **114** 9346–84
[59] Piyadasa A, Wang S and Gao P X 2017 *Semicond. Sci. Technol.* **32** 073001
[60] Moatti A, Sachan R, Kumar D and Narayan J 2019 *Acta Mater.* **167** 112–20
[61] Liu Q, Zhan H, Zhu H, Liu H, Sun Z, Bell J, Bo A and Gu Y 2019 *Nano Lett.* **19** 7742–9
[62] Freund H J and Pacchioni G 2008 *Chem. Soc. Rev.* **37** 2224–42
[63] Surnev S, Fortunelli A and Netzer F P 2013 *Chem. Rev.* **113** 4314–72
[64] Barcaro G and Fortunelli A 2019 *Phys. Chem. Chem. Phys.* **21** 11510–36
[65] Grinter D C, Yim C M, Pang C L, Santos B, Menteş T O, Locatelli A and Thornton G 2013 *J. Phys. Chem.* C **117** 16509–14
[66] Luches P and Valeri S 2015 *Materials (Basel)* **8** 5818–33
[67] Sauerbrey M, Gasperi G, Luches P, Falta J, Valeri S and Flege J I 2017 *Top. Catal.* **60** 513–21
[68] Blossey R 2003 *Nat. Mater.* **2** 301–6
[69] Weon S, He F and Choi W 2019 *Environ. Sci. Nano* **6** 3185–214
[70] Bach U, Lupo D, Comte P, Moser J E, Weissörtel F, Salbeck J, Spreitzer H and Grätzel M 1998 *Nature* **395** 583–5
[71] Sterrer M, Fischbach E, Heyde M, Nilius N, Rust H P, Risse T and Freund H J 2006 *J. Phys. Chem.* B **110** 8665–9
[72] Chang G S, Kurmaev E Z, Boukhvalov D W, Finkelstein L D, Kim D H, Noh T W, Moewes A and Callcott T A 2006 *J. Phys. Condens. Matter* **18** 4243–51
[73] Atrei A, Bardi U and Rovida G 1997 *Surf. Sci.* **391** 216–25
[74] Ashworth T V and Thornton G 2001 *Thin Solid Films* **400** 43–45
[75] Ashworth T V, Muryn C A and Thornton G 2005 *Nanotechnology* **16** 3041–4
[76] Papageorgiou A C, Cabailh G, Chen Q, Resta A, Lundgren E, Andersen J N and Thornton G 2007 *J. Phys. Chem.* C **111** 7704–10
[77] Papageorgiou A C, Pang C L, Chen Q and Thornton G 2007 *ACS Nano* **1** 409–14
[78] Guo Q, Oh W S and Goodman D W 1999 *Surf. Sci.* **437** 49–60
[79] Murphy S, Manai G and Shvets I V 2005 *Surf. Sci.* **579** 65–72
[80] Bennett R A, Poulston S, Stone P and Bowker M 1999 *Phys. Rev.* B **59** 10341–6
[81] Bennett R A 2000 *PhysChemComm* **3** 1–6
[82] McCarty K F and Bartelt N C 2003 *Surf. Sci.* **527** 3–7
[83] Rohrer G S, Henrich V E and Bonnell D A 1990 *Science* **250** 1239–41
[84] Calloni A, Ferrari A, Brambilla A, Ciccacci F and Duò L 2012 *Thin Solid Films* **520** 3922–6
[85] Raza H, Pang C L, Haycock S A and Thornton G 1999 *Phys. Rev. Lett.* **82** 5265–8
[86] Murray P W, Leibsle F M, Muryn C A, Fisher H J, Flipse C F J and Thornton G 1994 *Phys. Rev. Lett.* **72** 689

[87] Landree E, Marks L D, Zschack P and Gilmore C J 1998 *Surf. Sci.* **408** 300–9
[88] Klusek Z, Busiakiewicz A and Datta P K 2006 *Surf. Sci.* **600** 1619–23
[89] Fukushima K and Yamada I 1992 *Surf. Coat. Technol.* **51** 197–202
[90] Yamamoto S, Sumita T, Yamaki T, Miyashita A and Naramoto H 2002 *J. Cryst. Growth* **237–239** 569–73
[91] Yamamoto S, Nagata S, Takayama A and Yoshikawa M 2006 *Nucl. Instrum. Methods Phys. Res. Sect. B* **249** 374–6
[92] Sedona F, Eusebio M, Rizzi G A, Granozzi G, Ostermann D and Schierbaum K 2005 *Phys. Chem. Chem. Phys.* **7** 697–702
[93] Potapenko D V, Hrbek J and Osgood R M 2008 *ACS Nano* **2** 1353–62
[94] Artiglia L, Zana A, Rizzi G A, Agnoli S, Bondino F, Magnano E, Cavaliere E, Gavioli L and Granozzi G 2012 *J. Phys. Chem.* C **116** 12532–40
[95] Farstad M H, Ragazzon D, Walle L E, Schaefer A, Sandell A and Borg A 2015 *J. Phys. Chem.* C **119** 6660–9
[96] Luttrell T, Halpegamage S, Tao J, Kramer A, Sutter E and Batzill M 2015 *Sci. Rep.* **4** 1–8
[97] Diebold U, Ruzycki N, Herman G S and Selloni A 2003 *Catal. Today* **85** 93–100
[98] De Angelis F, Di Valentin C, Fantacci S, Vittadini A and Selloni A 2014 *Chem. Rev.* **114** 9708–53
[99] Burdett J K, Hughbanks T, Miller G J, Smith J V and Richardson J W 1987 *J. Am. Chem. Soc.* **109** 3639–46
[100] Apgar B A and Martin L W 2014 *Cryst. Growth Des.* **14** 1981–8
[101] Howard S A, Yau J K and Anderson H U 1989 *J. Appl. Phys.* **65** 1492–8
[102] Balluffi RW, Brokman A and King AH 1982 *Acta Metall.* **30** 1453–70
[103] Silva V F, Bouquet V, Députier S, Boursicot S, Ollivier S, Weber I T, Silva V L, Santos I M G, Guilloux-Viry M and Perrin A 2010 *J. Appl. Crystallogr.* **43** 1502–12
[104] Bickley R I, Gonzalez-Carreno T, Lees J S, Palmisano L and Tilley R J D 1991 *J. Solid State Chem.* **92** 178–90
[105] Connelly K, Wahab A K and Idriss H 2012 *Mater. Renew. Sustain. Energy* **1** 1–12
[106] Kafizas A, Carmalt C J and Parkin I P 2012 *Chem. A Eur. J.* **18** 13048–58
[107] Ma R and Chen T 2019 *J. Phys. Chem.* C **123** 19479–85
[108] Beinik I, Bruix A, Li Z, Adamsen K C, Koust S, Hammer B, Wendt S and Lauritsen J V 2018 *Phys. Rev. Lett.* **121** 206003
[109] Lazzeri M and Selloni A 2001 *Phys. Rev. Lett.* **87** 266105
[110] Lazzeri M, Vittadini A and Selloni A 2001 *Phys. Rev.* B **63** 1554091–9
[111] Shi Y, Sun H, Saidi W A, Nguyen M C, Wang C Z, Ho K, Yang J and Zhao J 2017 *J. Phys. Chem. Lett.* **8** 1764–71
[112] Xiong F, Yu Y Y, Wu Z, Sun G, Ding L, Jin Y, Gong X Q and Huang W 2016 *Angew. Chem. Int. Ed.* **55** 623–8
[113] Vitale E, Zollo G, Agosta L, Gala F, Brandt E G and Lyubartsev A 2018 *J. Phys. Chem.* C **122** 22407–17
[114] Xu M, Wang S and Wang H 2017 *Phys. Chem. Chem. Phys.* **19** 16615–20
[115] Xia Y, Zhu K, Kaspar T C, Du Y, Birmingham B, Park K T and Zhang Z 2013 *J. Phys. Chem. Lett.* **4** 2958–63
[116] Marchand R, Brohan L and Tournoux M 1980 *Mater. Res. Bull.* **15** 1129
[117] Banfield J F, Veblen D R and Smith D J 1991 *Am. Mineral.* **76** 343–53
[118] Armstrong A R, Armstrong G, Canales J and Bruce P G 2004 *Angew. Chem. Int. Ed.* **43** 2286–8
[119] Fehse M and Ventosa E 2015 *ChemPlusChem* **80** 785
[120] Ragazzon D, Farstad M H, Schaefer A, Walle L E, Uvdal P, Borg A and Sandell A 2015 *Surf. Sci.* **633** 102–8
[121] Vittadini A, Sedona F, Agnoli S, Artiglia L, Casarin M, Rizzi G A, Sambi M and Granozzi G 2010 *ChemPhysChem* **11** 1550–7
[122] Farstad M H, Ragazzon D, Grönbeck H, Strømsheim M D, Stavrakas C, Gustafson J, Sandell A and Borg A 2016 *Surf. Sci.* **649** 80
[123] Sandell A, Schaefer A, Ragazzon D, Farstad M H and Borg A 2017 *Surf. Sci.* **666** 104–12
[124] Yahia M B, Lemoigno F, Beuvier T, Jś F, Richard-Plouet M, Brohan L and Doublet M L 2009 *J. Chem. Phys.* **130** 204501
[125] Vittadini A, Casarin M and Selloni A 2009 *J. Phys. Chem.* C **113** 18973–7
[126] Finetti P, Sedona F, Rizzi G A, Mick U, Sutara F, Svec M, Matolin V, Schierbaum K and Granozzi G 2007 *J. Phys. Chem.* C **111** 869
[127] Zhang Y, Giordano L, Pacchioni G, Vittadini A, Sedona F, Finetti P and Granozzi G 2007 *Surf. Sci.* **601** 3488–96
[128] Sedona F, Sambi M, Artiglia L, Rizzi G A, Vittadini A, Fortunelli A and Granozzi G 2008 *J. Phys. Chem.* C **112** 3187–90
[129] Vittadini A and Casarin M 2008 *Theor. Chem. Acc.* **120** 551–6
[130] Sasaki T, Watanabe M, Hashizume H, Yamada H and Nakazawa H 1996 *J. Am. Chem. Soc.* **118** 8329–35
[131] Orzali T, Casarin M, Granozzi G, Sambi M and Vittadini A 2006 *Phys. Rev. Lett.* **97** 1–4
[132] Agnoli S, Orzali T, Sambi M, Vittadini A, Casarin M and Granozzi G 2008 *J. Phys. Chem.* C **112** 20038–49
[133] Atrei A, Ferrari A M, Szieberth D, Cortigiani B and Rovida G 2010 *Phys. Chem. Chem. Phys.* **12** 11587–95
[134] Harrison G T, Spadaro M C, Pang C L, Grinter D C, Yim C M, Luches P and Thornton G 2016 *Mater. Sci. Technol.* **32** 203–8
[135] Breinlich C, Buchholz M, Moors M, Le Moal S, Becker C and Wandelt K 2014 *J. Phys. Chem.* C **118** 6186–92
[136] Sato H, Ono K, Sasaki T and Yamagishi A 2003 *J. Phys. Chem.* B **107** 9824–8
[137] Tauster S J, Fung S C and Garten R L 1978 *J. Am. Chem. Soc.* **100** 170
[138] Tauster S J 1987 *Acc. Chem. Res.* **20** 389
[139] Fu Q, Wagner T, Olliges S and Carstanjen H D 2005 *J. Phys. Chem.* B **109** 944–51
[140] Sun Y M, Belton D N and White J M 1986 *J. Phys. Chem.* **90** 5178
[141] Sadeghi H R and Henrich V E 1984 *Appl. Surf. Sci.* **19** 330
[142] Tenney S A, He W, Roberts C C, Ratliff J S, Shah S I, Shafai G S, Turkowski V, Rahman T S and Chen D A 2011 *J. Phys. Chem.* C **115** 11112–23
[143] Suzuki T and Souda R 2000 *Surf. Sci.* **448** 33–39
[144] Steinrück H P, Pesty F, Zhang L and Madey T E 1995 *Phys. Rev.* B **51** 2427–39
[145] Pesty F, Steinrück H P and Madey T E 1995 *Surf. Sci.* **339** 83–95
[146] Dulub O, Hebenstreit W and Diebold U 2000 *Phys. Rev. Lett.* **84** 3646–9
[147] Pan J M and Madey T E 1993 *Catal. Lett.* **20** 269–74
[148] Óvári L and Kiss J 2006 *Appl. Surf. Sci.* **252** 8624–9
[149] Jennison D R, Dulub O, Hebenstreit W and Diebold U 2001 *Surf. Sci.* **492** L677
[150] Bennett R A, Pang C L, Perkins N, Smith R D, Morrall P, Kvon R I and Bowker M 2002 *J. Phys. Chem.* B **106** 4688–96
[151] Majzik Z, Balázs N and Berkó A 2011 *J. Phys. Chem.* C **115** 9535–44
[152] Berkó A, Gubó R, Óvári L, Bugyi L, Szenti I and Kónya Z 2013 *Langmuir* **29** 15868–77

[153] Gubó R, Óvári L, Kónya Z and Berkó A 2014 *Langmuir* **30** 14545–54
[154] Berkó A, Gubó R, Óvári L and Kónya Z 2015 *Surf. Sci.* **641** 300–4
[155] Sedona F, Rizzi G A, Agnoli S, Llabrés I Xamena F X, Papageorgiou A, Ostermann D, Sambi M, Finetti P, Schierbaum K and Granozzi G 2005 *J. Phys. Chem.* B **109** 24411–26
[156] Sedona F, Agnoli S and Granozzi G 2006 *J. Phys. Chem.* B **110** 15359–67
[157] Agnoli S, Barolo A, Finetti P, Sedona F, Sambi M and Granozzi G 2007 *J. Phys. Chem.* C **111** 3736–43
[158] Barcaro G, Sedona F, Fortunelli A and Granozzi G 2007 *J. Phys. Chem.* C **111** 6095–102
[159] Sedona F, Agnoli S, Fanetti M, Kholmanov I, Cavalire E, Gavioli L and Granozzi G 2007 *J. Phys. Chem.* C **111** 8024–9
[160] Barcaro G, Agnoli S, Sedona F, Rizzi G A, Fortunelli A and Granozzi G 2009 *J. Phys. Chem.* C **113** 5721–9
[161] Barcaro G, Fortunelli A, Granozzi G and Sedona F 2009 *J. Phys. Chem.* C **113** 1143
[162] Surnev S, Sock M, Kresse G, Andersen J N, Ramsey M G and Netzer F P 2003 *J. Phys. Chem.* B **107** 4777
[163] Sedona F, Granozzi G, Barcaro G and Fortunelli A 2008 *Phys. Rev.* B **77** 1–8
[164] Barcaro G, Cavaliere E, Artiglia L, Sementa L, Gavioli L, Granozzi G and Fortunelli A 2012 *J. Phys. Chem.* C **116** 13302–6
[165] Wu C, Marshall M S J and Castell M R 2011 *J. Phys. Chem.* C **115** 8643–52
[166] Mekata M 2003 *Phys. Today* **56** 12
[167] Männig A, Zhao Z, Rosenthal D, Christmann K, Hoster H, Rauscher H and Behm R J 2005 *Surf. Sci.* **576** 29–44
[168] Hutchings G J 1985 *J. Catal.* **96** 292–5
[169] Hashmi A S K and Hutchings G J 2006 *Angew. Chem. Int. Ed.* **45** 7896–936
[170] Haruta M, Kobayashi T, Sano H and Yamada N 1987 *Chem. Lett.* **16** 405–8
[171] Okumura M, Fujitani T, Huang J and Ishida T 2015 *ACS Catal.* **5** 4699–707
[172] Barcaro G, Fortunelli A and Granozzi G 2008 *Phys. Chem. Chem. Phys.* **10** 1876
[173] Artiglia L, Cavaliere E, Rizzi G A, Gavioli L and Granozzi G 2010 *J. Phys. Chem. Lett.* **1** 1660–5
[174] Artiglia L, Cavaliere E, Vascon A, Bondino F, Rizzi G A, Gavioli L and Granozzi G 2011 *J. Phys. Chem.* C **115** 15812–21
[175] Onishi H and Iwasawa Y 1994 *Chem. Phys. Lett.* **226** 111–4
[176] Grinter D C, Woolcot T, Pang C L and Thornton G 2014 *J. Phys. Chem. Lett.* **5** 4265–9
[177] Henderson M A, White J M, Uetsuka H and Onishi H 2003 *J. Am. Chem. Soc.* **125** 14974–5
[178] Henderson M A, White J M, Uetsuka H and Onishi H 2006 *J. Catal.* **238** 153–64
[179] Fujishima A and Honda K 1972 *Nature* **238** 37–38
[180] Henderson M A 2002 *Surf. Sci. Rep.* **46** 1
[181] Walle L E, Borg A, Uvdal P and Sandell A 2009 *Phys. Rev.* B **80** 1–5
[182] Blomquist J, Walle L E, Uvdal P, Borg A and Sandell A 2008 *J. Phys. Chem.* C **112** 16616–21
[183] Casarin M, Vittadini A and Selloni A 2009 *ACS Nano* **3** 317
[184] Muryn C A, Tirvengadum G, Crouch J J, Warburton D R, Raiker G N, Thornton G and Law D L 1989 *J. Phys. Condens. Matter* **1** SB127
[185] Muryn C A, Hardman P J, Crouch J J, Raiker G N, Thornton G and Law D S L 1991 *Surf. Sci.* **251-252** 747
[186] Rose M K, Mitsui T, Dunphy J, Borg A, Ogletree D F, Salmeron M and Sautet P 2002 *Surf. Sci.* **512** 48–60
[187] Harding D J, Neugebohren J, Hahn H, Auerbach D J, Kitsopoulos T N and Wodtke A M 2017 *J. Chem. Phys.* **147** 013939
[188] Neugebohren J *et al* 2018 *Nature* **558** 280–3
[189] Kuhn W K, Szanyi J and Goodman D W 1992 *Surf. Sci.* **274** L611
[190] Gao W, Choi A S and Zuo J M 2014 *Surf. Sci.* **625** 16–22
[191] Zuo J M, Shah A B, Kim H, Meng Y, Gao W and Rouviére J L 2014 *Ultramicroscopy* **136** 50
[192] Sivaramakrishnan S, Wen J, Scarpelli M E, Pierce B J and Zuo J M 2010 *Phys. Rev.* B **82** 1–10
[193] Ebert P 1999 *Surf. Sci. Rep.* **33** 121
[194] Roose B, Pathak S and Steiner U 2015 *Chem. Soc. Rev.* **44** 8326–49
[195] Stampe P A, Kennedy R J, Xin Y and Parker J S 2002 *J. Appl. Phys.* **92** 7114–21
[196] Chambers S A, Wang C M, Thevuthasan S, Droubay T, McCready D E, Lea A S, Shutthanandan V and Windisch J F 2002 *Thin Solid Films* **418** 197–210
[197] Ohsawa T, Yamamoto Y, Sumiya M, Matsumoto Y and Koinuma H 2004 *Langmuir* **20** 3018–20
[198] Batzill M, Katsiev K, Gaspar D J and Diebold U 2002 *Phys. Rev.* B **66** 1–10
[199] Batzill M, Hebenstreit E L D, Hebenstreit W and Diebold U 2003 *Chem. Phys. Lett.* **367** 319–23
[200] Yoon Y *et al* 2015 *ChemPhysChem* **16** 313–21
[201] Zheng J F, Liu X, Newman N, Weber E R, Ogletree D F and Salmeron M 1994 *Phys. Rev. Lett.* **72** 1490
[202] Ebert P, Heinrich M, Simon M, Domke C, Urban K and Shih C 1996 *Phys. Rev.* B **53** 4580–90
[203] Diebold U, Koplitz L V and Dulub O 2004 *Appl. Surf. Sci.* **237** 336–42
[204] Onoda J, Pang C L, Yurtsever A and Sugimoto Y 2014 *J. Phys. Chem.* C **118** 13674–9
[205] Schmid M, Hebenstreit W, Varga P and Crampin S 1996 *Phys. Rev. Lett.* **76** 2298
[206] Djukic D, Roth R M, Osgood R M, Evans-Lutterodt K, Bakhru H, Bakhru S and Welch D 2007 *Appl. Phys. Lett.* **91** 112906–9
[207] Yang L, Shu D J, Li S C and Wang M 2016 *Phys. Chem. Chem. Phys.* **18** 14833–9
[208] Bikondoa O, Pang C L, Ithnin R, Muryn C A, Onishi H and Thornton G 2006 *Nat. Mater.* **5** 189–92
[209] Wendt S, Matthiesen J, Schaub R, Vestergaard E K, Lægsgaard E, Besenbacher F and Hammer B 2006 *Phys. Rev. Lett.* **96** 1–4
[210] Pang C L, Sasahara A, Onishi H, Chen Q and Thornton G 2006 *Phys. Rev.* B **74** 073411
[211] Li S C, Zhang Z, Sheppard D, Kay B D, White J M, Du Y, Lyubinetsky I, Henkelman G and Dohnálek Z 2008 *J. Am. Chem. Soc.* **130** 9080–8
[212] Papageorgiou A C, Beglitis N S, Pang C L, Teobaldi G, Cabailh G, Chen Q, Fisher A J, Hofer W A and Thornton G 2010 *Proc. Natl Acad. Sci. USA* **107** 2391–6
[213] Zhang Z, Du Y, Petrik N G, Kimmel G A, Lyubinetsky I and Dohnálek Z 2009 *J. Phys. Chem.* C **113** 1908–16
[214] Matthiesen J *et al* 2009 *ACS Nano* **3** 517–26
[215] Zhang Z, Ge Q, Li S C, Kay B D, White J M and Dohnálek Z 2007 *Phys. Rev. Lett.* **99** 2–5
[216] Sánchez-Sánchez C, González C, Jelinek P, Méndez J, De Andres P L, Martín-Gago J A and López M F 2010 *Nanotechnology* **21** 405702
[217] Uwe H and Sakudo T 1976 *Phys. Rev.* B **13** 271
[218] Parker R A 1961 *Phys. Rev.* **124** 1719
[219] Traylor J G, Smith H G, Nicklow R M and Wilkinson M K 1971 *Phys. Rev.* B **3** 3457–72

[220] Samara G A and Peercy P S 1973 *Phys. Rev.* B **7** 1131–48
[221] Montanari B and Harrison N M 2004 *J. Phys. Condens. Matter* **16** 273–92
[222] Grünebohm A, Entel P and Ederer C 2013 *Phys. Rev.* B **87** 1–14
[223] Grünebohm A, Ederer C and Entel P 2011 *Phys. Rev.* B **84** 3–6
[224] Grünebohm A, Siewert M, Ederer C and Entel P 2012 *Ferroelectrics* **429** 31–42
[225] Ni L H, Liu Y, Ren Z H, Song C L and Han G R 2011 *Chin. Phys. B* **20** 106102
[226] Mitev P D, Hermansson K, Montanari B and Refson K 2010 *Phys. Rev.* B **81** 1–11
[227] Refson K, Montanari B, Mitev P D, Hermansson K and Harrison N M 2013 *Phys. Rev.* B **88** 2–6
[228] Grünebohm A, Ederer C and Entel P 2013 *Phys. Rev.* B **88** 136102
[229] Takahashi K, Takahashi L, Baran J D and Tanaka Y 2017 *J. Chem. Phys.* **146** 204104
[230] Wang M, Tan S, Cui X and Wang B 2019 *Acta Phys. Chim. Sin.* **35** 1412–21
[231] Tazaki R, Fu D, Itoh M, Daimon M and Koshihara S Y 2009 *J. Phys. Condens. Matter* **21** 215903
[232] Tao J, Luttrell T and Batzill M 2011 *Nat. Chem.* **3** 296–300
[233] Dette C, Pérez-Osorio M A, Kley C S, Punke P, Patrick C E, Jacobson P, Giustino F, Jung S J and Kern K 2014 *Nano Lett.* **14** 6533–8